

# Hollow cores in Warm Dark Matter halos from the Vlasov–Poisson equation

Claudio Destri

*Dipartimento di Fisica G. Occhialini,  
Università Milano-Bicocca  
and INFN, sezione di Milano-Bicocca,  
Piazza della Scienza 3, 20126 Milano, Italia.  
e-mail: claudio.destri@mib.infn.it  
(Dated: June 8, 2022)*

We report the results of extended high-resolution numerical integrations of the Vlasov–Poisson equation for the collapse of spherically symmetric WDM halos. For thermal relics with mass  $m = 1 \text{ keV}/c^2$ , we find collapsed halos with cores of size from 0.1 to 0.6 kpc. The typical core is hollow, with the mass density decreasing towards the core center by almost three orders of magnitude from its maximum near the core radius  $r_c$ . The core is in equilibrium with the diffused part of the halo but far from virialization. These properties are rooted in the conservation of the squared angular momentum and in the original excess, proper of WDM initial conditions, of kinetic energy in the core region. In a sample of more than one hundred simulated collapses, the values of  $r_c$  and of the core density  $\rho_c$  are in the range typical of dwarf spheroids, while the maximal circular velocities  $V_{\text{max}}$  are proper of small disk galaxies. The product  $\mu_c = \rho_c r_c$  takes values between  $116 M_\odot/\text{pc}^2$  and  $283 M_\odot/\text{pc}^2$ , while the surface density  $\mu_0$ , as determined from a Burkert fit, is roughly three times larger. From these data and data obtained at smaller values of  $m$ , we extrapolate for one particular halo  $\mu_c = 263(308) M_\odot/\text{pc}^2$  and  $\mu_0 = 754(855) M_\odot/\text{pc}^2$  at  $m = 2(3.3) \text{ keV}/c^2$ , to be compared with the observed value  $140_{-52}^{+83} M_\odot/\text{pc}^2$ . In view of the many improvements and enhancements available, we conclude that WDM is a viable solution for explaining the presence and the size of cores in low mass galaxies.

Keywords: cosmology: theory dark matter galaxies: halos methods: numerical

## Contents

<b>I. Introduction, summary and outlook</b>	2
A. Non-virialized hollow cores with nearly constant surface density	3
B. Directions for improvement	5
<b>II. Vlasov–Poisson equation</b>	6
A. VP equation for Dark Matter	7
B. VP equation with spherical symmetry	9
<b>III. Numerical setup</b>	10
A. Spherical symmetry and three-dimensional grids	11
B. Angular momentum	12
C. Boundary conditions	13
D. Initial configurations	13
E. On the CFL condition	14
F. Accuracy and stability tests	15
<b>IV. Main results</b>	17
A. Density and velocities	18
B. Core radius, surface density and other parameters	20
C. Potential and phase-space density	24
D. Non-virialized cores	26
E. Hollow cores and initial velocity dispersion	27
<b>Acknowledgments</b>	29
<b>References</b>	29

## I. INTRODUCTION, SUMMARY AND OUTLOOK

The investigation on how purely self-gravitating matter evolves on long time scales has played and still plays a central role in cosmology, in astrophysics and in statistical mechanics. From the statistical point of view, the main obstacle towards the establishment of a general picture is the lack of simple additivity due to the long range interaction. This prevents a system, even if composed by a macroscopic number of “particles”, to reach thermodynamic equilibrium, so that the usual laws of equilibrium thermodynamics do not apply [1]. Conversely, it is well known that there exist infinitely many stable equilibrium phase-space configurations to choose from as  $t \rightarrow \infty$  [2].

Still, relaxation of some sort must occur, since self-gravitating systems of many different kinds and sizes appear to be in (quasi-) stationary states [2, 3]. Likewise, numerical  $N$ -body simulations of such systems show that, from a coarse-grained point of view, some type of equilibration does occur [4]. The central issue is then how to properly identify the quasi-stationary states corresponding to given initial conditions. As detailed below, such identification is the aim of this work in the specific case of single Warm Dark Matter (WDM) halos, although the implications of our findings probably extend to wider domains.

Indeed, in the cosmological context, important questions concern the properties of DM halos, which are the cradles of galaxy formation [5]. In turn, the halos are formed through gravitational collapse triggered by tiny perturbations over the uniform DM background which dominates the total matter contribution  $\Omega_M \sim 0.3$  to the energy density of the Universe (baryons contributing only a smaller fraction  $\Omega_b \sim 0.04$ ). In this scenario, the counting and the properties of galaxies with any given mass should be traced back to the primordial power spectrum of DM perturbations, which statistically determines the initial conditions, and to the quasi-stationary state (or states) to which gravity drives the various local matter overdensities.

For example, in a Universe dominated by Cold Dark Matter (CDM) the density perturbations are gravitationally unstable down to mass scales much smaller than those of galaxies and extensive numerical simulations (see *e.g.* [6] and references therein) have shown that structure formation proceeds bottom-up with the early collapse of very small regions, followed by larger and larger ones, with a complex merging histories that produce successively more or less relaxed objects of increasing mass, like dwarf satellites, massive galaxies, groups and clusters. Thus the properties of a single DM halo depend on the full history of a much larger region of comoving space, hindering a clear-cut analytic modeling of its quasi-stationary state.

However, this CDM scenario has (at least) two distinguishing features contradicted by observations: it exhibits an overabundance of small mass virialized halos [7–11] and cuspy density profiles [12, 14] where observations point to cored ones [15–20]. The latter problem, the so-called cusp-core puzzle of CDM, apparently fades away upon including baryon feedback in certain simulations [21–23], but not in others [24, 25].

Structure formation based on WDM is in principle protected against these CDM difficulties, while reproducing all the observed large scale ( $\gtrsim 10$  Mpc) properties as CDM does. In fact WDM is characterized by the proper amount of primordial velocity dispersion, with associated free streaming, to smooth out initial density fluctuations over scales below the Mpc [26, 27]. This velocity dispersion should also help to better match the observed density profile of collapsed halos. In brief, WDM reconciles, or tend to reconcile with observations several small to middle scale astrophysical and cosmological features such as, for example, the halo concentration and satellite counts in  $N$ -body simulations [27, 28], the phase-space density of dwarf spheroids in a model-independent WDM treatment [29, 30], the mass function in the halo model [31], the galaxy luminosity functions and the stellar mass distributions in semi-analytic models [32]. Many other investigations [33–39] confirm that WDM agrees with observations better than CDM.

Still, one observational fact that many numerical simulations on WDM fail to correctly reproduce is the size of the halo cores [40–46]. Indeed, a well known theoretical argument, rooted on the Tremaine–Gunn bound [47], implies that WDM halos are cored [44, 48]. It is based on the so-called (pseudo) phase-space density [48–52],  $Q = \rho/\sigma^3$ , where  $\rho$  is the characteristic mass density and  $\sigma$  the characteristic one-dimensional velocity dispersion of the core. One can argue [48] (see [45, 53] for more punctual analysis that however do not alter significantly the conclusions) that  $Q < Q_{\text{prim}}$ , where the space-constant  $Q_{\text{prim}}$  is computed at WDM decoupling, in any given particle model. Then, *assuming* a halo model (*e.g.* an isothermal sphere as in ref. [48] or a pseudo-isothermal one as in ref. [44] to relate  $\sigma$  to  $\rho$ , one obtains a bound on the core size. WDM  $N$ -body simulations apparently produce cores which almost saturate this bound [44, 45]. The problem is that these cores are resolved, and found with size comparable to the observed ones, only for initial velocity dispersions so large that the corresponding free streaming would have erased at the linear level the fluctuation seeds of the halo themselves (the *catch 22* of ref. [44]). Viceversa, using the theoretical bound to extrapolate the size of resolved cores to velocity dispersions small enough to allow the fluctuation seeds, yields cores two order of magnitude smaller than the observed ones.

If this were indeed the situation, WDM structure formation would need help from baryon feedback (if that really can help) almost as badly as CDM does. Alternatively, it could be that current  $N$ -body simulations, plus extrapolations

based on equilibrium assumptions, do not provide a quantitatively sound description of WDM gravitational collapse below the kpc scale. Here we address the second possibility only and give an affirmative answer, by showing that WDM is an effective working hypothesis for explaining the size of observed DM cores.

In this work, we report the results of extensive high-resolution direct numerical integrations of the spherically symmetric Vlasov–Poisson equation for a 1 keV WDM thermal relic. The Vlasov–Poisson equation (2.1), often called collisionless Boltzmann–Poisson equation, describes the non-dissipative incompressible 6-dimensional phase-space flow of self-gravitating continuous matter. It is what  $N$ -body simulations attempt to approximately solve with fictitious particles moving in 3-dimensional configuration space.

Our findings, outlined in the next subsection and described in more detail in Sec. IV, provide an overall picture of WDM halo cores quite different from the commonly expected one, which is based on some apriori assumptions and the (extrapolation of the) results of  $N$ -body simulations.

### A. Non-virialized hollow cores with nearly constant surface density

A common expectation about cored DM halos, as those of WDM, is that their mass density is a monotonically decreasing function of  $r$  which has some core radius  $r_c$  as unique length scale in the core region. This is indeed the situation in collisionless self-gravitating systems at equilibrium, that are described by stationary and stable ergodic phase-space distributions [2]. The above expectation is then extended to quasi-stationary states, with the understanding that they do not differ much from truly equilibrium states. The property that should guarantee this proximity is core virialization, which can be described as follows.

Let us consider a spherical, purely self-gravitating system. Thanks to Gauss' law, one can unambiguously compute the gravitational potential energy  $U(r)$  within the sphere of radius  $r$ , regardless of the system configuration for  $r' > r$ . Hence one can define the  $r$ -dependent virial ratio  $W(r) = -2K(r)/U(r)$ , where  $K(r)$  is the kinetic energy within the sphere. Suppose the system has relaxed to some quasi-stationary state with a core of size  $r_c$ . For  $r$  large enough we expect virialization, that is  $W(r) \gtrsim 1$ . For  $r \ll r_c$  instead, we have  $W(r) \sim r^2$ , since  $K(r) \sim r^{-3}$  while  $U(r) \sim r^{-5}$  as  $r \rightarrow 0$  in a core that is in hydrostatic equilibrium. In between  $W(r)$  will decrease in some system-specific way. If  $W(r) \gtrsim 1$  for  $r/r_c \gtrsim 1$ , we can say that also the core is virialized. Since  $r_c$  is the only scale in the core region, also  $W(r)$  is a function only of  $x = r/r_c$ , which behaves as  $x^{-2}$  for  $x$  small enough and monotonically decreases in the interval  $0 < x \lesssim 1$ . This is exactly what happens for instance in the isothermal sphere and many other systems with ergodic phase-space distributions.

CDM halos do not have cores but are quite virialized, so they have only the system-specific decrease. For example, if we rather crudely assume  $\rho \sim r^{-1}$  à la NFW [12] and  $Q \sim r^{-1.9}$  [13], then  $W(r) \sim r^{-0.4}$ , in any case much slower than within a core.

WDM halos are cored and the  $r < r_c$  region can be theoretically and/or numerically investigated, provided the resolution is high enough. According to the common lore just described, the inner part of a halo should be in some quasi-stationary state not too different from stable equilibrium states. The halo core would then be virialized in the sense defined above.

On the contrary, the main result of our investigation can be stated as follow: *The spherical collapse of WDM yields cores that are hollow and not virialized.*

Details are provided in Sec. IV (see Figs. 1, 2 and 12 in particular). Here we just make few simple observations to support these numerical findings.

Let us assume for the moment that the inner part of the halo can indeed be modeled by some equilibrium-type cored configuration. Then for  $r \lesssim r_c$  we have  $W(r) \lesssim (r_c/r)^2$ , where  $r_c$  is in the kpc scale to match, for instance, the DM halos of dwarf galaxies.

Consider now the uniform isotropic Universe at some time  $t = t_0$  when the energy contribution of matter inhomogeneities is negligible and choose, in order to evaluate the initial value  $W_0(r)$  of the virial ratio, the center of a future collapse (of what type of DM does not matter yet) as origin of the comoving coordinates. The result is (see Sec. IV D for details on the elementary derivation):

$$W_0(r) = 2 + \frac{10\sigma_0^2}{a^4 H^2 r^2},$$

where  $a$  is the scale factor,  $H = \dot{a}/a$  is the Hubble parameter and  $\sigma_0$  is the DM (comoving) velocity dispersion. In the derivation we assumed that DM is non-relativistic at the time  $t_0$  considered.

In the case of CDM, we have  $\sigma_0 = 0$  and the gravitational collapse will need to reduce the nearly constant  $W_0$  by just a factor 2 to virialize the halo. Instead, in the case of WDM particles, that decouple while ultra-relativistic but

are already non-relativistic deep in the RD era, we obtain

$$W_0(r) \simeq 2 + 10 \left( \frac{l_{\text{fs}}}{r} \right)^2, \quad l_{\text{fs}} = (\Omega_r)^{-1/2} \frac{\sigma_0}{H_0},$$

where we used  $a^4 H^2 \simeq \Omega_R H_0^2$ , with  $\Omega_R$  the radiation fraction at time  $t = t_0$ , to recognize in  $l_{\text{fs}}$  a (very crude) estimation of the free-streaming length of the WDM particles. Therefore

$$\frac{W_0(r)}{W(r)} \simeq 10 \left( \frac{l_{\text{fs}}}{r_c} \right)^2, \quad r \lesssim r_c.$$

Indeed, by construction  $r_c \ll l_{\text{fs}}$ . For instance, thermal relics with a mass of  $1 \text{ keV}/c^2$  (and two internal degrees of freedom) have  $\sigma_0 = 0.025 \text{ km/s}$ , so that  $l_{\text{fs}} \simeq 40 \text{ kpc}$  since  $\Omega_R = 8.5 \times 10^{-5}$  by the time only neutrinos and photons contribute to radiation. Hence, throughout the region of the future core, kinetic energy initially exceeds by three orders of magnitudes the typical value it would eventually have in a few kpc virialized core. And the smaller the core, the higher the kinetic energy excess, since  $l_{\text{fs}}$  is fixed way before the collapse started.

Of course this is an idealized scenario, since the real collapse will not be spherical, there could be mergers and so on. But the free streaming of a keV-sized WDM has also the merit of smoothing out the matter fluctuations on scales of several hundreds kpc. Then the possibility of a nearly spherical and almost undisturbed collapse is certainly not a far-fetched idealization as it would be for CDM. Hence the kinetic energy excess in the initial conditions w.r.t. the virialized core after the collapse holds beyond the approximation of spherical symmetry.

During the collapse, phase mixing and violent relaxation [74] alone might still bring the system to a quasi-stationary state but, lacking more efficient energy transfer mechanisms such as radiation or dissipation, they need not be able to reduce the virial ratio by the thousands in the finite amount of time available. This is just what we observe by numerically integrating the Vlasov-Poisson equation.

A complementary viewpoint is based on the conservation of angular momentum, which is the same in physical and comoving coordinates. In a spherically symmetric system, the 1-particle angular momentum is conserved also if the potential is not constant. Of course, the mean vector angular momentum vanishes by symmetry, but the squared angular momentum  $\ell^2$  does not. Matter which is initially at a distance  $R \gg r_c$  but will eventually fall in the core, has a conserved  $\ell^2$  of order  $(R\sigma_0)^2$ . Like the skate dancer that closes her arms, this matter will spin faster in the core, sustaining the original excess of core kinetic energy.

The net result we observe and describe in Sec. IV, is the formation of halos with a hollow core, that is with a non monotonically decreasing mass density which develops its maximum  $\rho_{\text{max}}$  at some  $r_{\text{max}} > 0$ , which provides a first natural definition of core radius. Throughout the core and beyond a large excess of kinetic energy is trapped mostly in tangential motions. The core is approaching a dynamic rather than hydrostatic equilibrium and the mass density  $\rho(r)$  features a roughly parabolic rise till  $r_{\text{max}}$ , where  $\rho_{\text{max}}$  is almost three order of magnitude larger than the density deep into the core. For  $r > r_{\text{max}}$ ,  $\rho(r)$  quite rapidly settles to the  $r^{-2}$  decrease that implies a constant circular velocity. Clearly the crossover at  $r = r_{\text{max}}$  provides another length scale beside  $r_{\text{max}}$ .

We find that these properties are common to all the 111 halos of our sample. The halos are obtained starting from different initial overdensity profiles, which are in turn constructed, according to the procedure described in Sec. III D, by angle averaging over the peaks of a random realization of the fluctuation field proper of a 1 keV WDM thermal relic. The overall shape of  $\rho(r)$  is almost independent of the initial conditions and of the location or value of the maximum itself (see Figs. 1, 2 and 3). These latter quantities instead, which fix the overall scale of  $\rho(r)$ , do depend on the details of the the initial fluctuation profile, such as height and size.

The hollow core shape allows a natural definition of the core radius  $r_c$  and the core density  $\rho_c$  slightly different from  $(r_{\text{max}}, \rho_{\text{max}})$ : the pair  $(r_c, \rho_c)$  define the point where the density  $\rho(r)$  should be cut to replace the hollow core with a constant density core (see Sec. IV B).  $r_c$  is therefore slightly larger than  $r_{\text{max}}$ .

In our sample we find values of  $r_c$  ranging from 0.1 to 0.6 kpc and values of  $\rho_c$  ranging from 0.2 to  $2.5 M_\odot/\text{pc}^3$ . Very interestingly, the core radius  $r_c$  is nearly inversely proportional to the core density  $\rho_c$  leading to an nearly constant value of  $\mu_c \equiv \rho_c r_c$  around  $210 M_\odot/\text{pc}^2$  (see Sec. IV B for more details), in remarkable agreement with the observations reported in refs. [54–57]. However, while the near constancy of  $\mu_c$  could be rooted in the core hollowness (a constant surface density means a constant core mass per unit area, a property certainly more appropriate to hollow cores than to bulky ones), the quantitative proximity to the observational value  $\mu_{0,\text{obs}} = 140_{-52}^{+83} M_\odot/\text{pc}^2$  is rather puzzling (and quite intriguing), since the estimation of  $\mu_{0,\text{obs}}$  is based on the hypothesis that the DM density has a bulky Burkert profile [58], with its own definition of core radius  $r_{0\text{B}}$  and core density  $\rho_{0\text{B}}$ . When a Burkert fit is performed on the hollow cores for  $r_c \lesssim r \lesssim 10 r_c$  (see Sec. IV B for the details), one obtains values of  $\mu_0 \equiv \rho_{0\text{B}} r_{0\text{B}}$  around  $600 M_\odot/\text{pc}^2$ , roughly four times larger than  $\mu_{0,\text{obs}}$ .

The typical  $r_c$  we find is more than one order of magnitude larger than what expected for a WDM particle of mass  $m = 1 \text{ keV}/c^2$  according to the  $Q$ -based theoretical bound and extrapolations from resolved cores of  $N$ -body simulations [44, 45, 48]. But this type of arguments rely on the a priori assumption of a *thermalized*, and a *fortiori* virialized, core and therefore is not applicable to the WDM cores found in our simulations. See Sec. IV B for the explicit comparison of the hollow core with that of the isothermal sphere, which shows in detail how the isothermal extrapolation fails; see Sec. IV E for our technical explanation of why it fails.

On the other hand, at odd with  $N$ -body simulations, our halos feature a diffuse part with a  $r^{-2}$  tail which is too long. The density is still decreasing almost as slowly as  $r^{-2}$  where it takes values from 100 to 200 times larger than the critical density. One possible cause is a bias in our construction of spherically symmetric overdensity profiles for the initial conditions (see Sec. III D), which does not allow enough matter outflow from the collapsing halo. This makes it awkward to build a reliable  $r_c$  vs.  $M_{\text{halo}}$  relation, for any common definition of halo mass  $M_{\text{halo}}$ .

Hence, as in observations, the best way to quantify the mass content of a halo is to consider the maximal circular velocity  $V_{\text{max}}$ . In our sample we find that  $V_{\text{max}}$  takes values between 50 to 70 km/s, characteristic of small disk galaxies, whereas  $r_c$  and  $\rho_c$  are typical of dwarf spheroids. This concentration excess is properly measured by means of the Burkert fit for  $r_c \lesssim r \lesssim 10 r_c$ . We find that  $r_{\text{cB}}$  is roughly twice  $r_c$ , while  $V_{\text{B,max}}$ , the maximal circular velocity of the Burkert fit, is always very close to  $V_{\text{max}}$ . Hence, apart from the mass deficit of the hollow core w.r.t. the Burkert core for  $r < 0.5 r_{\text{cB}}$ , our halos differ from realistic DM halo only because the surface density  $\mu_0$  is four times larger than the observed value. In other words, the region  $0.5 r_{\text{cB}} \lesssim r \lesssim 5 r_{\text{cB}}$  of our hollow-core halos is more concentrated than real DM halos by a factor roughly equal to 4. In Sec. IV E we estimate that this factor grows to 5 when the mass of the WDM particle is raised up to  $m = 2 \text{ keV}/c^2$ , the value that now seems most favored [59, 60], and reaches 6 when  $m = 3.3 \text{ keV}/c^2$ , the lower bound from Lyman- $\alpha$  and hydrodynamical simulations of ref. [61].

This quantitative analysis is the least restrictive, since the Burkert fit is performed only for  $0.5 r_{\text{cB}} \lesssim r \lesssim 5 r_{\text{cB}}$ , the only region of the inner halo where the fit can be accurate. Since the bulky Burkert profile provides a very good fit to real DM halos down to few percents of  $r_{\text{cB}}$ , the hollow core is most likely ruled out observations. Hence whatever improvement, modification and/or enhancement that might succeed in reducing  $\mu_0$  should also eliminate, or strongly reduce, the hollowness. An obvious addition could be baryons, completely neglected in the zeroth order approach of this work and possible hollowness-reducer thorough adiabatic compression. Another could be quantum corrections, to be briefly motivated in the next section.

At any rate, since we find cores with an inner mass deficit rather than excess, with a surface density nearly constant and relatively close to the observed value, the starting point provided by our VP approach appears by far better than in CDM-only  $N$ -body simulations or in the too-small-core WDM simulations cited above.

In the next section we outline some improvements for our WDM-only VP simulations and we also question the soundness of another common a priori assumption on DM dynamics.

## B. Directions for improvement

The first, obvious and major improvement would be to go beyond the approximation of spherically symmetric collapse and tackle the full 6-dimensional Vlasov-Poisson problem. A promising low-resolution attempt in this direction is reported in ref. [62], but the computational resources required for a high-resolution cosmological simulation appear at the moment prohibitively large, at least for the author. Moreover, it is very unlikely that the problem  $\mu_0/\mu_{0,\text{obs}} \sim 4$  is entirely due to the approximation of spherical symmetry.

Remaining in the more tractable framework of spherical symmetry, we can consider a few interesting directions for future improvement:

1. A problematic aspect of our halo sample is the small variation of the basic parameters  $\rho_c$ ,  $r_c$  and  $V_{\text{max}}$ . The most likely cause is a bias in our construction of spherically symmetric overdensity profiles for the initial conditions (see Sec. III D), which does not allow enough matter outflow from the collapsing halo. A more sophisticated selection procedure could be implemented to better mimic, even within the approximation of spherical symmetry, the effects of nearby collapsing halos on the halo of interest. This could at the same time increase the parameter variations and reduce the too long  $r^{-2}$  tail of the halos. It is also conceivable that a shorter  $r^{-2}$  tail could improve the value of the surface density  $\mu_0$ , although probably less than necessary.
2. The large initial virial ratio and the crucial role played by angular momentum imply that the halo collapse might be sensitive to details of the freeze-out velocity distribution, which in our simulation we fixed to the simplest Fermi-Dirac form proper for thermal relics (see Sec. II A). Indeed we find that the core properties strongly depend on  $\sigma_0$  (see Sec. IV E). Hence other WDM models, which are already known to yield different cutoff effects on the primordial power spectrum [63–66], might also lead to noticeable effects on the core properties. In this

respect, accurate analysis at the linear level also of WDM velocities, as that in ref. [67], could play an important quantitative role in the collapse dynamics through a better determination of the initial conditions.

3. Another common a priori assumption on DM dynamics, besides the core virialization discussed above, is that quantum effects are fully negligible. The large density variation in the hollow core, the crucial role played by angular momentum in our WDM collapse and the profound quantum modifications to the theory of angular momentum, suggest instead that Quantum Mechanics could have a deep role in the shaping of WDM cores, provided its effects were non negligible in the primordial Universe. We elaborate this point below. The relevance of Quantum Mechanics for ultra-compact dwarf galaxies with WDM halos, within an equilibrium approach, was discussed already in ref. [68].

For a particle of mass  $m$ , the quantum unit of phase-space density is

$$q = \frac{m^4}{(2\pi\hbar)^3} = 5.13 \times 10^{-4} \left( \frac{mc^2}{\text{keV}} \right)^4 \frac{M_\odot}{\text{pc}^3} (\text{km/s})^{-3}.$$

Strictly speaking it should just be  $(2\pi\hbar)^{-3}$ , the inverse of the volume of a quantum cell in the phase space with the conventional dimensions of  $(\text{length} \times \text{momentum})^3$ . The extra factor of  $m^4$  comes from the normalization to a mass density, rather than a number density, and to the use of velocity rather than momentum as coordinate in phase space. If  $g$  denotes the number of non-translation degrees of freedom of the particle, such as spin and/or internal symmetry quantum numbers, it follows that (notice the  $(2\pi)^3/g$  difference w.r.t. ref. [68])

$$\frac{Q}{gq} = \frac{(2\pi\hbar)^3 \rho}{g m^4 \sigma^3} = \frac{1}{g} \left( \frac{\lambda_{\text{dB}}}{d} \right)^3, \quad \lambda_{\text{dB}} = \frac{2\pi\hbar}{m\sigma}, \quad d = \left( \frac{m}{\rho} \right)^{1/3}$$

where  $\lambda_{\text{dB}}$  is the characteristic de Broglie wavelength and  $d$  is the mean interparticle distance. Thus  $Q/(gq)$  provides a semiclassical measure of how much particles in a non-relativistic gas with density  $\rho$  and velocity dispersion  $\sigma$  are packed w.r.t. the reference quantum packing fixed by Heisenberg's indetermination principle. Values  $\gtrsim 1$  of  $Q/(gq)$  then indicate that quantum effects could be important, as in the standard non-relativistic free Fermi gas.

Since  $Q$  largely decreases during the classical gravitational collapse (we verified this also in our simulations, see Sec. IV C), we have to compare it with  $gq$  at the beginning, when WDM is already non-relativistic but still nearly homogeneous. For thermal relics the issue is solved in the simplest possible way, since in that case the primordial value of  $Q/(gq)$  is a pure number that does not depend on cosmological parameters nor on the actual value of the mass: [29, 30, 48]:

$$\frac{Q_{\text{prim}}}{gq} = 4\pi\sqrt{27} \frac{I_2^{5/2}}{I_4^{3/2}} = 2.52950728 \dots, \quad I_n \equiv \int_0^\infty \frac{x^n dx}{1+e^x}.$$

Thus the classical framework might not be fully adequate for WDM, after all. If so, also the history before should be revisited to determine more appropriate initial conditions with the necessary quantum corrections, Namely, the classical framework ignores from the start the fermionic quantum pressure which, in view of the above value of  $Q_{\text{prim}}$ , could significantly contrast the gravitational pull and flatten the halo cores, as advocated in refs. [68, 69].

## II. VLASOV-POISSON EQUATION

In the mean-field approximation, the phase-space one-particle distribution function  $f(\mathbf{r}, \mathbf{v}, t)$  of a purely self-gravitating system of  $N$  identical particles evolves according to the Vlasov-Poisson (VP) equation

$$\begin{aligned} [\partial_t + \mathbf{v} \cdot \nabla_r + (\nabla_r \Phi) \cdot \nabla_v] f &= 0, \\ \nabla_r^2 \Phi &= 4\pi G \rho, \quad \rho(\mathbf{r}, t) = \int d^3v f(\mathbf{r}, \mathbf{v}, t). \end{aligned} \tag{2.1}$$

Here  $\rho$  represent the mass density of the system, obviously normalized as

$$\int d^3r \rho(\mathbf{r}, t) = Nm \equiv M,$$

where  $m$  is the particle mass. Strictly speaking then, it is  $f/m$  that plays the role of one-particle distribution function. Mean-field approximation means that two-body or higher correlation functions are considered always negligible. Then

the specific value  $m$  of the particle mass drops completely out of the game if  $f$  is normalized as in eqs. (2.1), which now describe the evolution of a non-dissipative incompressible fluid in phase space subject only to the self-consistent gravitational force it generates. In fact, the first equation in (2.1) is nothing but Liouville's equation for free streaming in the "external" field  $\Phi$ .

It is commonly believed (and in a certain special sense rigorously demonstrated [73]) that in the limit  $N \rightarrow \infty$  the mean-field description becomes exact. But from the more practical point of view of understanding the dynamics of the  $10^{70}$  (or more) particles of a DM halo, for example, there can be little doubt that the self-gravitating fluid description implied by the mean-field approximation is more accurate than any  $N'$ -body dynamics with  $N'$  at least  $10^{60}$  times smaller than  $N$  and simulation "particles" as massive as  $10^4 M_\odot \sim 10^{50} \text{ GeV}/c^2$ . Due to the absence of dissipative phenomena in the collisionless mean-field dynamics, it is legitimate to have doubts also on the hydrodynamic approximations to eqs. (2.1), where the moment expansion in velocity space is closed at second order by some heuristic equation of state.

The problem, from a numerical point of view, is that simulations of the six-dimensional continuous system eqs. (2.1), without any symmetry to help, are much more demanding than  $N'$ -body or 3-dimensional hydrodynamical simulations.

Since the Vlasov equation is formally time-reversible, the system retains full memory of its initial conditions, albeit dispersed on smaller and smaller scales over phase space. It is commonly believed that any reasonably coarse-grained version of the exact solution  $f(\mathbf{r}, \mathbf{v}, t)$  does relax to some form of equilibrium, or quasi-stationary states (QSS), a typical feature of systems with long-range interactions. Lynden-Bell theory of violent relaxation [74–76] provides a rather general framework for this, although only for very special situations it has been possible to verify that the QSS to which the system relaxes does indeed maximize the Lynden-Bell coarse-grained entropy [77, 78].

In other words, little is known on the class of initial conditions that do lead to QSS, or, if the system does relax to QSS, on the map from the space of initial conditions to the space of QSS and on the relative time scales. However, this fact is not a major issue in the cosmological applications of the VP equation, since the initial conditions in the linear regime of the gravitational clustering are rather well known. Then the real problem is to solve as accurately as possible the VP equation and see what really happens in the finite cosmic time available, regardless of any assumed relaxation to a QSS.

### A. VP equation for Dark Matter

In the cosmological FRW spacetime, well after matter-radiation equilibration, the non-relativistic DM fluid evolves according to VP system (2.1) of Newtonian equations, with  $t$  identified with the cosmic time. But in a cosmological context one cannot ignore the (accelerated) universe expansion even for a single DM halo. If the phase-space coordinates  $(\mathbf{r}, \mathbf{v})$  are interpreted as physical coordinates for a DM particle, then no change is needed in eqs. (2.1) to implement a decelerated expansion, since the latter affects only the initial conditions through the assumption of the proper Hubble flow. On the other hand, the accelerated expansion caused by the cosmological constant  $\Lambda$  requires to introduce antigravity, by appropriately changing the source term in Poisson's equation, that is

$$\nabla_{\mathbf{r}}^2 \Phi = 4\pi G(\rho - 2\rho_\Lambda), \quad (2.2)$$

where

$$\rho_\Lambda = \Omega_\Lambda \rho_{\text{crit}}, \quad \rho_{\text{crit}} = \frac{3 H_0^2}{8\pi G}$$

is the energy density due to  $\Lambda$ , written in terms of the present fraction  $\Omega_\Lambda$  and of the critical density or, equivalently, of the present Hubble parameter  $H_0$ . Here we neglect the other smaller source of Newtonian potential, namely baryons, so that  $\Omega_{\text{DM}} = \Omega_{\text{M}}$  and  $\Omega_\Lambda = 1 - \Omega_{\text{M}} \simeq 0.7$  if  $\Omega_{\text{M}} \simeq 0.3$  is the total matter fraction.

Actually, a more convenient framework is obtained by using comoving coordinates and the superconformal time  $s$  in place of the cosmic time  $t$ . We first rename  $(\mathbf{r}, \mathbf{v})$  to  $(\mathbf{r}_{\text{phys}}, \mathbf{v}_{\text{phys}})$  and  $\rho$  to  $\rho_{\text{phys}}$ ; then we set

$$\mathbf{r}_{\text{phys}} = a\mathbf{r}, \quad \mathbf{v}_{\text{phys}} = H\mathbf{r}_{\text{phys}} + \frac{\mathbf{v}}{a}, \quad H \equiv \frac{\dot{a}}{a}, \quad \rho_{\text{phys}} = a^{-3}\rho, \quad dt = a^2 ds$$

where  $a$  is the scale factor, solution of the acceleration equation of uniform expansion

$$\frac{\ddot{a}}{a} = \frac{4\pi G}{3} \left( \frac{\rho_{\text{M}}}{a^3} - 2\rho_\Lambda \right), \quad \rho_{\text{M}} \equiv \Omega_{\text{M}} \rho_{\text{crit}} \quad (2.3)$$

and upper dots denote as usual derivative w.r.t.  $t$ . In terms of the comoving  $(\mathbf{r}, \mathbf{v})$  and the superconformal time  $s$  the VP system of equations now reads

$$[\partial_s + \mathbf{v} \cdot \nabla_r + (\nabla_r \phi) \cdot \nabla_v] f = 0, \quad (2.4)$$

where  $\phi$  is  $a^2$  times the potential due solely to fluctuation over the uniform background, that is

$$\begin{aligned} \Phi &= \Phi_M + \Phi_\Lambda + a^{-2} \phi, & \Phi_M &= \frac{2\pi G}{3a} \rho_M r^2, & \Phi_\Lambda &= -\frac{4\pi G}{3} \rho_\Lambda a^2 r^2 \\ \nabla_r^2 \phi &= 4\pi G a \left[ \int d^3 u f(\mathbf{x}, \mathbf{u}, s) - \rho_M \right]. \end{aligned} \quad (2.5)$$

The time dependence of the scale factor is fixed by Eq. (2.3), or by the equivalent Friedmann equation in superconformal time

$$a^2 H = \frac{1}{a} \frac{da}{ds} = H_0 \sqrt{\Omega_\Lambda a^4 + \Omega_M} \quad (2.6)$$

We see that, apart from the different symbol interpretation, the Liouville part of the VP system is the same as before and the Universe expansion is equivalent to introducing a negative matter background and time dependency on the gravitational coupling. The background due to the cosmological constant drops out of the game and  $\Omega_\Lambda$  directly affects only the evolution of the scale factor.

To complete this dynamical setup, we have to provide the initial conditions for eqs. (2.4) and (2.6). We assume that at  $s = 0$  the scale factor is  $a = a_i = (1 + z_i)^{-1}$ , with the initial redshift  $z_i$  large enough so that DM is well within the linear regime and the distribution function has to a very good approximation the factorized form

$$f(\mathbf{r}, \mathbf{v}, s = 0) = \rho_M [1 + \delta_i(\mathbf{r})] f_i(|\mathbf{v} + \nabla\psi(\mathbf{r})|) \quad (2.7)$$

Here the overdensity fluctuation field  $\delta_i$  is a random realization of the Gaussian process with the matter power spectrum at redshift  $z_i$ , while  $f_i(|\mathbf{v}|)$  is the frozen-out distribution, that is the unit-normalized space-uniform isotropic velocity distribution at decoupling which would remain constant in the uniform Universe, that is if  $\delta_i = 0$ .  $\psi$  is the potential for the initial average velocity field (the Zeldovich velocity) and satisfies

$$\nabla_r^2 \psi = a_i^2 \dot{\delta}_i \simeq a_i^2 H(a_i) \delta_i = H_0 \delta_i (1 + z_i)^{-1/2} \sqrt{\Omega_M + \Omega_\Lambda (z_i + 1)^{-3}}$$

in order to fulfill to first order in  $\delta_i$  the mass continuity equation

$$\partial_s \rho + \nabla \cdot (\rho \langle \mathbf{v} \rangle) = 0, \quad \langle \mathbf{v} \rangle(\mathbf{r}, s) \equiv \frac{1}{\rho(\mathbf{r}, s)} \int d^3 v \mathbf{v} f(\mathbf{r}, \mathbf{v}, s)$$

at the initial time.

The specification of the matter power and of the frozen-out distribution  $f_i$  characterizes the type of DM. In the case of CDM the power spectrum has a slow power-like falloff at small scales while  $f_i(\mathbf{v})$  is for all practical purposes a delta function at  $\mathbf{v} = 0$ . In the case of WDM the power spectrum is more or less (depending on the specific WDM model) sharply cut off at scales smaller than the DM free-streaming length, while  $f_i(\mathbf{v})$  is a (highly model-dependent) isotropic distribution. Here we consider only a specific model of WDM, namely fermionic thermal relics that decoupled at thermal equilibrium while ultrarelativistic, so that, if  $f_{\text{FD}}$  denotes the dimensionless Fermi-Dirac distribution, we have [27, 48]

$$\rho_M f_i(\mathbf{v}) = q f_{\text{FD}}(\epsilon) = q \frac{g}{1 + e^{\epsilon/T}}, \quad q \equiv \frac{m^4}{(2\pi\hbar)^3}, \quad (2.8)$$

where  $\epsilon = mc|\mathbf{v}|$  is the kinetic energy,  $T$  is the (comoving) decoupling temperature and  $g$  is the number of non-translational degrees of freedom of the DM particle, such as spin and/or internal symmetry quantum numbers. For example,  $g = 2$  or  $g = 4$ , depending on the specific model, in the case of a serious spin-1/2 candidate for WDM such as the sterile neutrino [70–72].

From Eq. (2.8) we can derive the following expression for the frozen-out velocity distribution ( $v = |\mathbf{v}|$  and  $\zeta(x)$  is Riemann's  $\zeta$ -function):

$$\begin{aligned} f_i(v) &= \frac{A(B/\sigma_0)^3}{1 + e^{Bv/\sigma_0}}, & 3\sigma_0^2 &= 4\pi \int_0^\infty dv v^4 f_i(v) \\ A &= \frac{1}{6\pi \zeta(3)} = 0.04413405\dots, & B &= \left[ \frac{5\zeta(5)}{\zeta(3)} \right]^{1/2} = 2.0768098\dots, \end{aligned} \quad (2.9)$$



with the identifications

$$\rho_{\text{M}} A \left( \frac{B}{\sigma_0} \right)^3 = g q, \quad T = \frac{m c \sigma_0}{B}.$$

Thus, recalling that  $\rho_{\text{M}} = \Omega_{\text{M}} \rho_{\text{crit}}$ , we obtain a rewriting of the relation of refs. [27, 48] between the mass and the velocity dispersion of the WDM particle (notice that  $v_0 = \sigma_0/B$  is most often quoted in the literature)

$$\sigma_0 = 0.025 \left( \frac{h}{0.7} \right)^{2/3} \left( \frac{\Omega_{\text{M}}}{0.3} \right)^{1/3} \left( \frac{2}{g} \right)^{1/3} \left( \frac{\text{keV}}{m c^2} \right)^{4/3} \text{ km/s}. \quad (2.10)$$

For what concerns the explicit choice of the WDM power spectrum, details are provided in section III D.

### B. VP equation with spherical symmetry

The solution of the full six-dimensional VP equation presents a major challenge, both from the analytical and numerical point of view. Analytical results are restricted to perturbation theory and partial resummation thereof (see *e.g.* ref. [79] and references therein), while numerical results are only preliminary [62].

The numerical study of the collapse of a single spherically symmetric system is much more tractable, while retaining a great interest both theoretically and from the point of view of its applications to concrete physical contexts.

If the DM distribution function is rotational invariant, we can use as independent phase-space variables  $r = |\mathbf{r}|$ ,  $u = (\mathbf{r}/r) \cdot \mathbf{v}$  and the conserved squared angular momentum (per unit mass)  $\ell^2 = |\mathbf{r} \wedge \mathbf{v}|^2 = r^2 (|\mathbf{v}|^2 - u^2)$ . Then

$$f = f(r, u, \ell^2, s) \quad , \quad \rho(r, s) = \frac{\pi}{r^2} \int_{-\infty}^{\infty} du \int_0^{\infty} d\ell^2 f(r, u, \ell^2, s) \quad (2.11)$$

and the VP equations read

$$\left[ \partial_s + u \partial_r + \left( \frac{\ell^2}{r^3} - \phi' \right) \partial_u \right] f = 0 \quad , \quad \phi'(r, s) \equiv \partial_r \phi(r, s) = \frac{G a}{r^2} \left[ M(r, s) - \frac{4\pi}{3} \rho_{\text{M}} r^3 \right] \quad (2.12)$$

where

$$M(r, s) = 4\pi \int_0^r dr' r'^2 \rho(r', s),$$

is the total dark mass within a sphere of radius  $r$ . No derivative w.r.t.  $\ell^2$  may appear in the left hand of Eq. (2.12) because  $\ell^2$  is a conserved quantity in this collisionless dynamics.

In this spherically symmetric framework, the moment expansion of the VP equation is obtained by multiplying it by integer powers of  $u$  and  $\ell^2$  and then integrating over  $u$  and  $\ell^2$ . Using the standard notation of expectation values

$$\mathcal{M}_{k,n}(r, s) = \langle u^k \ell^{2n} \rangle \equiv \frac{\int_{-\infty}^{\infty} du \int_0^{\infty} d\ell^2 u^k \ell^{2n} f(r, u, \ell^2, s)}{\int_{-\infty}^{\infty} du \int_0^{\infty} d\ell^2 f(r, u, \ell^2, s)}$$

and after one integration by parts in  $u$ , one obtains

$$\partial_t (\rho \mathcal{M}_{k,n}) + \frac{1}{r^2} \partial_r (r^2 \rho \mathcal{M}_{k+1,n}) = k \rho \left( \frac{1}{r} \mathcal{M}_{k-1,n+1} - \phi' \mathcal{M}_{k-1,n} \right), \quad k, n = 0, 1, 2, \dots, \quad (2.13)$$

with the convention that  $\mathcal{M}_{-1,n} \equiv 0$ . When  $k = n = 0$  one has the mass continuity equation with spherical symmetry

$$\partial_t \rho + \frac{1}{r^2} \partial_r (r^2 \bar{u} \rho) = 0, \quad \bar{u} = \mathcal{M}_{1,0} = \langle u \rangle,$$

while if  $k = 1, n = 0$  and the continuity equation is used, one obtains Euler (or momentum) equation

$$(\partial_t + \bar{u} \partial_r) \bar{u} + \frac{1}{\rho} \partial_r (\rho \sigma_r^2) + \frac{2}{r} (\sigma_r^2 - \sigma_\theta^2) + \phi' = 0, \quad (2.14)$$

where

$$\sigma_r^2 = \mathcal{M}_{2,0} - \mathcal{M}_{1,0}^2 = \langle u^2 \rangle - \bar{u}^2, \quad \sigma_\theta^2 = \frac{\mathcal{M}_{0,1}}{2r^2} = \frac{\langle \ell^2 \rangle}{2r^2} \quad (2.15)$$

are the squared radial and tangential velocity dispersions, respectively. In the Cartesian frame the pressure tensor reads

$$P_{jk} = \rho \sigma_\theta^2 \delta_{jk} + \rho (\sigma_r^2 - \sigma_\theta^2) \frac{r_j r_k}{r^2} \quad (2.16)$$

and the vectorial form of Eq. (2.14) can be recovered by setting  $\bar{u}_j = \bar{u} r_j / r$ .

In a quasi-stationary state with slowly varying hydrodynamic variables  $\rho$  and  $\bar{u}$ , Euler equation (2.14) implies that wherever  $\bar{u} = 0$  we must also have

$$\frac{1}{\rho} \partial_r (\rho \sigma_r^2) + \frac{2}{r} (\sigma_r^2 - \sigma_\theta^2) + \phi' = 0, \quad (2.17)$$

which is known as Jeans equation in the astrophysical context. From the fluid point of view, the condition  $\bar{u} = 0$  is the marker of hydrostatic equilibrium. On the other hand, for the gas of individual particles orbiting in the slowly varying potential  $\phi$ , the definition of *dynamic* equilibrium is perhaps more appropriate. Only in the isotropic limit  $\sigma_r^2 = \sigma_\theta^2 \equiv P/\rho$ ,  $P_{jk} = P \delta_{jk}$ , Jeans equation reduce to the equation of simple hydrostatic equilibrium  $\partial_r P = -\rho \phi'$ .

To be useful, the infinite hierarchy in Eq. (2.13) needs to be approximately closed at some order, but with no obvious physical basis for collisionless DM. On the other hand, if effective collisional terms were added on some physical grounds, the induced dissipation would allow to write an effective equation of state to relate the pressure (then quickly rendered isotropic by dissipation) to the density and perhaps the local entropy. DM is collisionless and only more complex mechanisms, such as the effects of localized DM clumps acting like macro-particles, could allow reliable closures at higher order such as those in ref. [80]. Numerous clumps at many small scales are indeed present in CDM bottom-up clustering, but they most likely do not play an important role for WDM, due to the much smoother initial conditions. Tackling the full hierarchy, that is the original VP equation, appears then mandatory for WDM.

The initial conditions in Eq. (2.7) take now the form

$$f(r, u, \ell^2, s = 0) = \rho_M [1 + \delta_i(r)] f_i(\sqrt{[u - u_i(r)]^2 + \ell^2/r^2}), \quad (2.18)$$

where  $u_i(r)$  is the initial infall velocity

$$u_i(r) = -\frac{\delta M_i(r)}{4\pi \rho_M r^2} (1 + z_i)^{-1/2} \sqrt{\Omega_M + \Omega_\Lambda (z_i + 1)^{-3}} \quad (2.19)$$

written in terms of the overmass

$$\delta M_i(r) = 4\pi \rho_M \int_0^r dr' r'^2 \delta_i(r'). \quad (2.20)$$

We see that the spherical symmetry has allowed to reduce the problem to three dimensions. Of these, two dimensions correspond to the radial phase space with coordinates  $(r, u)$ . The third coordinate  $\ell^2$  enters the VP equation in (2.12) as a constant parameter, but is to be integrated over to obtain the density as in Eq. (2.11).

### III. NUMERICAL SETUP

Let us consider the Vlasov equation (2.4) regarding first  $-\nabla\phi$  as an external time-independent acceleration field. This is just the Liouville equation for the incompressible streaming of any conserved local quantity in the phase-space of a single particle. The formal solution can be written

$$f(s) = e^{sL} f(0), \quad L = L_r + L_v, \quad L_r = -\mathbf{v} \cdot \nabla_r, \quad L_v = (\nabla_r \phi) \cdot \nabla_v$$

where  $L$  is the so-called Liouvillian operator. Of course  $L_r$  and  $L_v$  do not commute and  $e^{sL}$  cannot be factorized into the product of exponentials of  $L_r$  and  $L_v$ . But we can certainly write

$$e^{sL} = [e^{\tau L}]^n, \quad s = n\tau \quad (3.1)$$

and for  $\tau \rightarrow 0$

$$e^{\tau L} = e^{\tau \tilde{L}(\tau)} + O(\tau^3), \quad e^{\tau \tilde{L}(\tau)} \equiv e^{\tau L_v/2} e^{\tau L_r} e^{\tau L_v/2} \quad (3.2)$$

The cubic order or the approximation can be checked by brute force power expansion of the exponentials or, more simply, by noticing that

$$e^{-\tau \tilde{L}(\tau)} = [e^{\tau \tilde{L}(\tau)}]^{-1} = e^{-\tau L_v/2} e^{-\tau L_r} e^{-\tau L_v/2} = e^{-\tau \tilde{L}(-\tau)}$$

implies

$$\tilde{L}(\tau) = \tilde{L}(-\tau) = L + O(\tau^2).$$

Furthermore it should be noticed that

$$e^{s \tilde{L}(\tau)} = e^{-\tau L_v/2} [e^{\tau L_v} e^{\tau L_r}]^n e^{\tau L_v/2}$$

and therefore one needs to alternatively apply many times  $e^{\tau L_v}$  and  $e^{\tau L_r}$ , while  $e^{\pm \tau L_v/2}$  only once at the beginning and the end. Notice also that we may exchange the role of  $L_r$  and  $L_v$  in  $\tilde{L}(\tau)$  without any problem. This yields a second approximate evolution whose proximity to the first one can be used to check the accuracy of both methods.

The promotion of  $-\nabla\phi$  to a time-dependent acceleration field that depends on  $f$  itself is rather straightforward: we need just to calculate  $-\nabla\phi$  from the Poisson equation just before every time  $e^{\tau L_v}$  is applied. In the application to the cosmological context of eqs. (2.4) and (2.5) the gravity strength is also growing in time with the scale factor  $a$ . We found that better stability in the evolution is obtained by choosing non-uniform  $s$ -steps corresponding to uniform steps in  $a$ , as can easily be determined from Eq. (2.6).

The great advantage of the well known operator splitting [82] defined in Eq. (3.2) is that the half-step evolution operators,  $e^{\tau L_v}$  or  $e^{\tau L_r}$ , are just  $\mathbf{r}$ -dependent translations in  $\mathbf{v}$  or  $\mathbf{v}$ -dependent translations in  $\mathbf{r}$ . With the so-called finite volume methods [82] these translations (which correspond to the so-called *advection* equation) can be implemented very accurately on uniform as well as non-uniform grids on phase space, in such a way to ensure machine-precision local conservation of the  $f$  values at each update. That is, the  $\mathcal{L}_1$  norm of  $f$  in any portion of the grid changes only because of the flows at its boundaries. On the other hand, the  $\mathcal{L}_n$  norms with  $n > 1$ , which are all exactly conserved in the continuum, are only approximately conserved on any finite grid, unavoidably implying a numerical coarse graining. In the continuum also the squared modulus of the  $f$  Fourier transforms in  $\mathbf{r}$  and/or  $\mathbf{v}$ , is conserved. This ceases to apply after discretization, unless one makes use of the non-local translation algorithm based on the discrete fast Fourier transform. This algorithm, however, is more demanding in terms of computer power and is essentially restricted to uniform grids; a serious limitation, as we shall see, in the present case of gravitational collapse.

Generally speaking all Vlasov solvers, that is numerical methods that solve directly the Vlasov equation on a phase-space grid, are free of the noise inherent to  $N$ -body simulations but suffer to one degree or another of numerical artifacts, like diffusion and dissipation. In ref. [81] a comparison of different solvers was performed in the case of a two-dimensional phase space. No method was found as a clear winner, especially when the dependence of the acceleration on the density is considered, as necessary in the VP system (in [81] the context is that of plasma physics, but there a close similarity to the cosmological setup in comoving coordinates). In fact, the semi-Lagrangian methods with large integration time steps, which are certainly less diffusive of those based on operator splitting plus finite volumes, are not allowed when the acceleration field changes with time in a way that depends on the solution itself.

Altogether, provided diffusion and dissipation are under control, the simplicity and stability of operator splitting and finite volume methods makes them particularly suited for the purposes of this work. All numerical results reported in the sequel as based on such a method. In particular, we have chosen a high-resolution finite volume advection solver based on the piecewise linear reconstruction with total-variation-decreasing slope limiters [82]. A similar choice was made in ref. [62], where the first (low resolution) simulations in the full six-dimensional phase space are reported.

### A. Spherical symmetry and three-dimensional grids

As already stated above, in this work we restrict our attention to the spherical symmetric case of section II B. The phase space is then two-dimensional and, together with the angular momentum  $\ell^2$ , we have a three-dimensional setup. Thus high resolutions can be achieved. To obtain spherically symmetric initial conditions, we perform averages

over angles of the initial distribution  $f(\mathbf{r}, \mathbf{v}, s = 0)$  of Eq. (2.7) around suitably chosen points as discussed in more detail below.

Some caution is necessary in the treatment of the squared angular momentum  $\ell^2$ , which of course needs to be discretized too. The actual values used, and in particular their total number, must be chosen wisely depending on the  $(r, u)$  phase-space grid (see subsection III B). The latter cannot really be a static uniform grid, since the gravitational collapse spans too many dynamical scales. In this case, where the collapse center is fixed beforehand, it is simpler to opt for a static non-uniform grid which gets finer and finer near  $r = 0$  and  $v = 0$ . Of course, in a higher-dimensional situation when the collapse centers are not known apriori, the most sensible choice would be to use some adaptive mesh refinement scheme.

High resolution requires indeed non-uniform grids. The radial density grows by several orders of magnitude near the origin and the detailed evolving structure of this peak is just the subject of this study. At the same time radial velocities become very large near the collapse center and the grid must allow for them since the only conceivable boundary conditions in velocity space are those of free outflow and no inflow. A grid with a too small velocity cutoff would lead to unphysical mass loss. A non-uniform grid may allow for a large velocity cutoff while keeping within reason the total number of cells in the  $u$  direction.

We used non-uniform phase-space grids which have  $n_r \times n_u$  cells, with  $n_r$  ranging from 400 to 700 and  $n_u$  from 600 to 1000, to select the best compromise between resolution and speed. These cells have increasing width both for increasing  $r$  and  $|u|$ , with the exponential laws  $\Delta x_{j+1} = (1 + \epsilon_x)\Delta x_j$  for  $x = r, u$  and  $0.015 < \epsilon_r < 0.028$ ,  $0.02 < \epsilon_u < 0.03$ , both variable parameters in search of the best compromise between resolution and speed. The narrowest cells in  $r$ , which are adjacent to  $r = 0$ , have typical widths around 2 pc and the narrowest cells in  $u$ , which are adjacent to  $u = 0$ , have typical widths around 2 m/s. The grid setup in the  $\ell^2$ -direction is described next.

## B. Angular momentum

The conservation of angular momentum plays a crucial role in the spherically symmetric collapse and must be handled very carefully. The angular momentum content of the system is fixed once and for all by the initial distribution  $f_i(r, u, \ell^2)$  in Eq. (2.18) and we need to numerically perform the integral over  $\ell^2$  in Eq. (2.12) with a level of accuracy which is consistent with the chosen  $(u, v)$ -grid. Since  $f_i(r, u, \ell^2, s)$  dies exponentially fast for large  $\ell^2$ , the integral can be cutoff at some finite value maintaining the desired accuracy. Much trickier is the discretization near  $\ell^2 = 0$ .

Indeed, from Eq. (2.11) and Eq. (2.8), we see that

$$\int_{-\infty}^{\infty} du \int_0^{\infty} d\ell^2 f_i(r, u, \ell^2) = \frac{r^2}{\pi} \quad (3.3)$$

while  $f_i(r, u, \ell^2, s)$  dies exponentially fast in  $1/r^2$  for any  $\ell^2 > 0$ . Still, the condition (3.3) should be fulfilled as closely as possible on the cell centers of the  $r$ -grid when the integral over  $u$  and  $\ell^2$  are replaced by finite sums. Moreover, one should worry also about the higher  $u$ -moment versions of (3.3). The higher  $\ell^2$ -moment versions are not as worrisome, since the various  $\ell^2$ -components are coupled only through their sum.

In our mass-conserving finite-volume setup, the integral over  $u$  is naturally replaced by the sum over  $u$ -cells properly weighted by the cell widths. For the sum  $\ell^2$  we have more freedom but, for obvious computational reasons, this sum should be as small as possible. To reach a convenient compromise, we adopted a Gaussian quadrature scheme with few free parameters which were optimized to fulfill Eq. (3.3) to a given order for all cell centers of the  $r$ -grid. For grids with 400  $r$ -cells with the first cell, adjacent to  $r = 0$ , of width  $\sim 2$  pc, uniform agreement to order  $10^{-3}$  requires a costly  $\ell^2$ -grid with several thousands of points, where  $\ell^2 = O(1)$  pc<sup>2</sup> (m/s)<sup>2</sup> is the smallest value, that is few times smaller than the angular momentum discretization scale corresponding to the  $(u, v)$ -grid.

Fortunately, the  $\ell^2$ -grid can be substantially coarsened by the following simple strategy: as far as the initial conditions are concerned, we can relax the accurate fulfillment of Eq. (3.3) and start with a coarser  $\ell^2$ -grid by including in Eq. (2.7) a suitable compensating factor  $\kappa(r)$ ;  $\kappa(r)$  cannot anyway be too different from unity, since it allows to preserve the initial overmass, but cannot prevent the inaccuracy in higher  $u$ - and  $\ell^2$ -moments of  $f_i$ . Of course this trick is not possible during the evolution, since we do not know beforehand the r.h.s. in Eq. (3.3) when  $f(r, u, \ell^2, s)$  replaces  $f_i(r, u, \ell^2)$  in the l.h.s.; we just have to run few prototype cases with finer and finer  $\ell^2$ -grids, with correspondingly  $\kappa(r)$  closer and closer to unity, until the evolution stabilizes. Typically, this happens more or less when the number of  $\ell^2$  values reaches that of  $r$  values. The corresponding  $\kappa(r)$  exceeds unity by few percents for all but the first and/or second leftmost  $r$ -grid center, where it can reach values up to 10. In spite of this we could verify in the prototype cases, by measuring against long runs with thousands of  $\ell^2$  values, that the numerical evolution remains quite accurate even on those cells.

### C. Boundary conditions

Boundary conditions must be set also at  $r = 0$  and at some finite value  $R_{\max}$  of  $r$ . On the line  $r = 0$  the correct condition is of reflecting type, with each half  $r$ -line at a given  $u > 0$  and the corresponding half  $r$ -line at  $u < 0$  “glued” together so that  $r$ -translations act smoothly at  $r = 0$ . Finally, at  $r = R_{\max}$  we assume free outflow, while the inflow can be null or free. The last two alternatives are actually quite different, since with no inflow the total mass can only decrease with time, while with free inflow it might go both ways depending on the initial conditions. In the cosmological context free inflow appears more natural, since the system under study is just a very small portion of an initially nearly uniform Universe.

On the other hand, owing to the presence of the background mass in Eq. (2.12), it is possible to essentially decouple the DM halo from the rest of the Universe, thus rendering the two alternatives of null or free inflow almost indistinguishable. To this end, it is sufficient to set up the initial fluctuation profile  $\delta_i(r)$  in Eq. (2.18) in such a way that the overmass  $\delta M_i(r)$  of Eq. (2.20) vanishes at some point  $r = R_0 < r_{\max}$ . Then the initial infall velocity  $u_i(r)$  also vanishes at  $r = R_0$  and in the first stages of evolution DM flow away from  $R_0$  in both directions. For the rest of the evolution till redshift zero, a small but rather stable outward flux for  $R_0 < r < R_{\max}$  is maintained by the gravitational push in the under dense region and by the free outflow conditions at  $r = R_{\max}$ . This prevents in a physical way any uncontrolled inflow at  $r = R_{\max}$  when inflow is allowed by the boundary conditions.

### D. Initial configurations

As anticipated at the end of section II A, we assume for the initial velocity distribution  $f_i(v)$  the Fermi–Dirac form of Eq. (2.9) proper for fermions. that decoupled at equilibrium while ultrarelativistic.  $f_i(v)$  parametrically depends only on the initial one-dimensional velocity dispersion  $\sigma_0$  given by Eq. (2.10). Typically, in our simulations we made the most straightforward reference choice  $h = 0.7$ ,  $\Omega_M = 0.3$ ,  $g = 2$  and  $m = 1$  keV, so that  $\sigma_0 = 25$  m/s.

To complete the determination of  $f(r, u, \ell^2, s = 0)$  in Eq. (2.18), we need instances of the initial overdensity profile  $\delta_i(r)$ , from which also the initial infall velocity  $u_i(r)$  can be determined according to Eq. (2.19). One possibility is to make use of the reknown results of ref. [83] on the local peak statistics of random Gaussian fields. We prefer here to proceed in a purely numerical fashion, to avoid the averaging of local peak profiles over all random field realizations.

We set the initial redshift as  $z_i = 100$  (and verified that  $z_i = 200$  led to almost indistinguishable results) and then followed the following procedure:

1. Compute the WDM power spectrum  $P(k)$  for fermionic thermal relics of the given mass (1 keV/ $c^2$ ) at redshift  $z = z_i$ , using (a slight modification of) the 2011 CAMB package [84]. Analytic expressions like those in refs. [27, 85] could be used with almost unnoticeable effects on the simulations.
2. Extract a random Gaussian field  $g(\mathbf{r})$  over a cubic lattice (we used two lattices, one with  $512^3$  points and a lattice spacing of 45 kpc, the other with  $768^3$  points and a spacing of 22 kpc), with zero mean and unit (in the sense of Kronecker’s delta) variance.
3. Fast-Fourier transform  $g(\mathbf{r})$ , multiply the result by  $P(k)$  and inversely Fast-Fourier transform this product to obtain one realization of the fluctuation field  $\delta_i(\mathbf{r})$  on the original lattice;
4. Repeat the previous step multiplying the Fourier transform of  $g(\mathbf{r})$  by  $W(kR)\sqrt{P(k)}$ , where  $W(kR)$  is the Fourier transform of the sharp window function  $[3/(4\pi R^3)]\theta(R - r)$ , namely

$$W(y) = \frac{3}{y^3} (\sin y - y \cos y)$$

and  $R$  is chosen with an eye to the characteristic mass  $(4\pi/3)\rho_M R^3$  of collapsed halos (but see below for more); then inversely Fast-Fourier transform to obtain a smoothed  $\delta_{i,R}(\mathbf{r})$  realization of the fluctuation field. Obviously  $\delta_i(\mathbf{r})$  and  $\delta_{i,R}(\mathbf{r})$  differ significantly only if  $R$  is significantly larger than the WDM free-streaming length, which for a 1 keV/ $c^2$  thermal relic can be calculated to be 185 kpc [66].

5. Select local maxima of  $\delta_{i,R}(\mathbf{r})$  which are *prominent*, that is, which are higher than all other peaks within a distance  $R'$  to be properly selected (see below).
6. Perform a spherical average of the unsmoothed  $\delta_i(\mathbf{r})$  around these prominent maxima and then interpolate over the chosen  $(r, u)$ -grid to obtain the radially symmetric peaked profiles  $\delta_i(r)$  to use in Eq. (2.18) and Eq. (2.19).

Some comments are required on the procedure just outlined. First of all let us stress that the aim is not really at an accurate halo statistics, for which more sophisticated approaches are needed. Rather, we try and produce several initial spherically symmetric peak profiles that are at least compatible with the true initial conditions, which are certainly not spherically symmetric. In this respects, certain common interpretations require some adjustment, especially because of the higher smoothness of the WDM fluctuation fields  $\delta_i(\mathbf{r})$  w.r.t. those of CDM.

For instance, in our approach the relation between the smoothing scale  $R$  and the mass  $\bar{M}(R) = (4\pi/3)\rho_M R^3$  of collapsed halos is just marginal. Only after the collapse, at redshift  $z = 0$ , we can measure the actual mass of each DM halo and this typically turns out to be larger than  $\bar{M}(R)$ . In fact, to trust the spherical symmetry approximation, it is necessary that a collapse center be sufficiently isolated, bringing in the other distance scale  $R'$  characterizing the prominence as in point 5 above. By its definition,  $R'$  must be chosen quite larger than  $R$ , but not necessarily as proportional to  $R$ . The mass of a collapsed halo is in between  $\bar{M}(R)$  and  $\bar{M}(R')$  and depends on specific features, as shown in Sec. IV A, of the initial overdensity profile  $\delta_i(r)$ . The chosen value of  $R$ , which must be in any case larger than the free-streaming length, sets an approximate lower bound on the halo mass and allows for collapse centers that are not maxima of the unsmoothed fluctuation field  $\delta_i(\mathbf{r})$ . Notice indeed that the initial profiles  $\delta_i(r)$  are often not monotonically decreasing nor maximal at  $r = 0$ , although a common feature of all profiles is their overall decrease toward zero (which is the average of the fluctuation field) at larger distances, as dictated by the spherical average and the prominence requirement. The latter also implies that quite often  $\delta_i(r)$  becomes negative sufficiently far away. In turns, this often causes the corresponding overmass  $\delta M_i(r)$  to vanish at some slightly larger distance.

In the upper panels of Fig. 1 we show a small subsample of initial fluctuation peaks obtained by the procedure outlined above, together with the corresponding overmass. In the lower panel we anticipate the form of the collapsed halos. The distance  $R_0$  at which  $\delta M_i(r)$  vanishes determines  $M_0 = (4\pi/3)\rho_M R_0^3$ , the total amount of DM mass potentially involved in the collapse, which in turns provides an upper limit to the mass of the collapsed halo for whatever definition of such a mass one may choose. Sometime the overmass does not vanishes within the simulation interval  $0 < r < R_{\max}$ , in which case we modify by hand the far end of the  $\delta_i(r)$ , through the addition of a negative Gaussian peak centered near  $R_{\max}$ , in order to determine a value of  $R_0$  close to  $R_{\max}$ . As explained in Sec. III C the vanishing of  $\delta M_i(R_0)$  allows to decouple the collapsing halo from the rest of the Universe, preventing on physical basis a uncontrolled inflow rather than just setting the inflow to zero as a sharp (and unphysical) boundary condition. On the other hand, all initial peak profiles for which the arrangement by hand is necessary have essentially the same value of  $M_0$ . This feature, together with selection of peaks by prominence (and probably several other reasons), quite likely makes our sample of initial conditions statistically biased.

### E. On the CFL condition

Named after Courant, Friedrichs, and Lewy, this is a necessary condition of stability (and hence convergence) for any numerical method that aims at solving partial differential equations (PDE). It can be formulated as “A numerical method can be convergent only if its numerical domain of dependence contains the true domain of dependence of the PDE” [82]. In the case of linear as well as non-linear transport equations, this requirement is often translated into a bound of the form

$$\nu \equiv \left| \frac{w \Delta t}{\Delta x} \right| \leq 1 \quad (3.4)$$

on the so-called *Courant number*  $\nu$ . Here  $\Delta x$  represents the cell width of a one-dimensional grid with a generic  $x$  coordinate,  $\Delta t$  is the integration timestep and  $w$  is the advection, or transport, velocity. To be more precise, there are in general as many bounds like the one above as there are cells, and with time dependence too, since  $\Delta x$ ,  $\Delta t$  and  $w$  might all have a local nature, due to non-uniformity of the grid, adaptive integration stepping and most notably dependence of  $w$  on the PDE unknowns when the transport equation is non-linear.

In our case  $x$  is either  $r$  or  $u$ ,  $w$  is one of the corresponding advection velocities in Eq. (2.12)

$$w_r = u, \quad w_u = \frac{\ell^2}{r^3} - \phi'(r, s)$$

while  $\Delta t$  is to be identified with the superconformal timestep  $\tau$  of Eq. (3.1). Then the bound in Eq. (3.4) becomes prohibitively stringent at small values of  $r$  and/or large values of  $u$ , imposing values too small for  $\tau$ , with uncontrollable diffusion and dissipation. This would indeed constitute a major obstacle to the whole approach if the bound on the Courant number was regarded as necessary for the CFL condition to hold.

In reality, however, the bound of Eq. (3.4) applies only to local updating algorithms, that is methods in which the updated value of the variable of interest in a given cell depends on the old values in the same cell and in a small, fixed

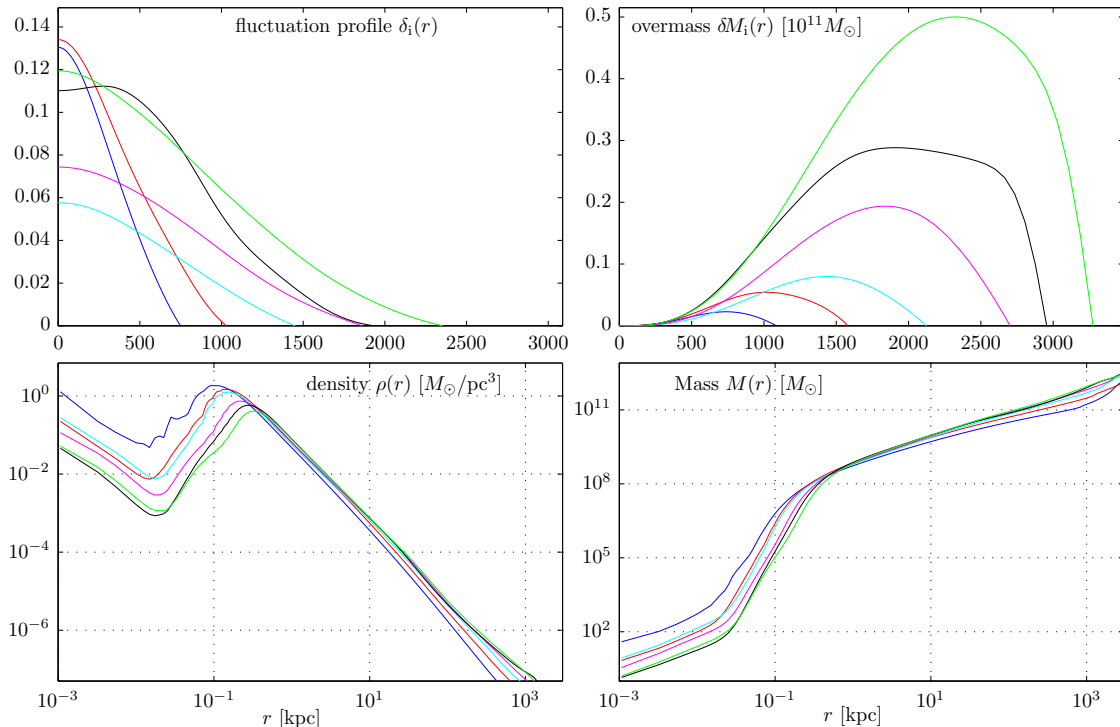


FIG. 1: Upper panels: initial profiles, at redshift  $z = 100$ , for six different realizations of the procedure described in Sec. III D. Lower panels: density and mass at redshift  $z = 0$ , after the collapse.

number (which depends on the specific method) of nearby cells (the so-called algorithm stencil). The bound does not apply to non-local algorithms where the stencil grows with the advection velocity.

The simplest example is uniform advection in one dimension. In this case advection reduces to rigid translation; then, if the lattice is uniform, by splitting the translation parameter into an integer multiple of the lattice spacing  $\Delta x$  plus the fractional part, one can advect in a single step by amounts  $w\Delta t$  much larger than  $\Delta x$ , making the Courant number  $\nu$  arbitrarily large. Using piecewise linear reconstruction, it is not difficult to extend this method also to non-uniform lattices. Finally, since as explained above, the operator-splitting Vlasov solver reduces to intertwined translations, we can forget about the bound of Eq. (3.4) on the Courant number and freely choose the superconformal timesteps in order to minimize diffusion and dissipation while maintaining accuracy.

## F. Accuracy and stability tests

To check our algorithms against numerical artifacts we performed several stability and accuracy tests on the core advection solver as well as on the full program. For brevity, we report here only the main results of three full-program tests. Indeed, the advection solver was adapted from quite standard, widely tested and employed algorithms (see *e.g.* ref. [82] and reference therein).

As accuracy quantifiers we considered the relative  $\mathcal{L}_1$ -norm, that is

$$\Delta_X = \frac{\sum_k w_k |X_k^{(m)} - X_k^{(e)}|}{\sum_k w_k |X_k^{(e)}|}$$

where  $X$  is either the distribution  $f$  itself or  $M(r)$  (mass),  $K(r)$  (kinetic energy),  $U(r)$  (potential energy) computed for the sphere of radius  $r$ .  $X^{(m)}$  stands for the measured value while  $X^{(e)}$  stands for the one expected on theoretical grounds. The sum runs over all indices of the observable, that is all grid indices in case of  $f$  or only the  $r$  indices in case of  $M$ ,  $K$  and  $U$ . The weights  $w_k$  are the cell volumes or widths in the  $r$ -direction, respectively. The data reported in Table I refer to a  $n_r \times n_u \times n_{\ell_2}$  grid with  $n_r = 400$ ,  $n_u = 600$  and  $n_{\ell_2} = 432$ . Similar grids were used for most collapse simulations.

	$\Delta_M$		$\Delta_K$		$\Delta_U$		$\Delta_f$	
test 1	$2.8 \times 10^{-4}$	$8.5 \times 10^{-3}$	$5.2 \times 10^{-3}$	$1.7 \times 10^{-2}$	–	–	$2.3 \times 10^{-2}$	0.1
test 2	$1.8 \times 10^{-2}$	$6.3 \times 10^{-2}$	0.6	0.25	$5.7 \times 10^{-2}$	0.47	$0.9 \times 10^{-2}$	0.15
test 3	$2.2 \times 10^{-4}$	$3 \times 10^{-3}$	$1.6 \times 10^{-4}$	$1.3 \times 10^{-3}$	$2.8 \times 10^{-4}$	$1.2 \times 10^{-3}$	$7.5 \times 10^{-2}$	1.58

TABLE I: Results of the test simulations described in Sec. III F. For each quantifier the two column report the values at  $t = T/10$  and  $t = T$ , except for test 3, for which they correspond to redshift  $z = 16$  and  $z = 0$ .

#### Test 1: Free streaming

This first test is just on free streaming, namely, without expansion nor gravity. The trivial analytic solution  $f(\mathbf{r}, \mathbf{v}, t) = f(\mathbf{r} - \mathbf{v}t, \mathbf{v}, 0)$  can be turned into a general rule for the  $f(r, u, \ell^2, t)$  of the spherical setup, but its implementation on the  $(r, u)$ -grid requires rather intricate interpolations. We therefore consider an initial distributions of factorized form  $f(r, u, \ell^2, 0) = \rho_i(r)f_i(v)$ , so that we immediately have the analytic form of  $f^{(e)}$ , that is

$$f(r, u, \ell^2, t) = \rho_i(r')f_i(v), \quad r'^2 = r^2 + 2rut + \left(u^2 + \frac{\ell^2}{r^2}\right)t^2.$$

In particular we take  $\rho_i(r)$  and  $f_i(v)$  to be both Gaussians with zero mean and width  $w_0$  and  $\sigma_0$ , respectively. As time span for the evolution we take  $T = \sqrt{3}w_0/\sigma_0$ , which is the time needed for the spatial width to double. From Table I one can see that the accuracy on  $M$ ,  $K$  and  $U$  profiles is very good even if numerical diffusion is affecting  $f$  quite substantially.

#### Test 2: King sphere

This test checks the numerical stability of a King sphere, as in ref. [62], so that the  $X^{(e)}$  are just the initial values of the  $X^{(m)}$ . In a notation slightly different from that in refs. [2, 62], we have

$$f(r, u, \ell^2, 0) = C\theta(\psi)(e^\psi - 1), \quad \psi = \psi_0 - \frac{1}{2\sigma^2} \left[ u^2 + \frac{\ell^2}{r^2} + 2\Phi(r) \right],$$

where  $\theta(x)$  is the step function,  $C$  is a constant that fixes the total finite mass  $M$  of the system,  $\sigma$  is the central velocity dispersion,  $\psi_0$  is King's shape parameter and  $\Phi(r)$  is the self-consistent potential. This ergodic phase-space distribution is stationary and stable, but any numerical VP integrator inevitably changes it. The smallness of the change, which necessarily grows in time due to numerical diffusion and dissipation, is a measure of the accuracy and stability of the integrator.

To be definite, we set  $\psi_0 = 8$  and choose the two scale parameters  $C$  and  $\sigma$  so that, if  $r_0$  is the King radius and  $\rho_0$  is the central density, then  $r_0 = 4.77$  kpc and  $\rho_0 r_0 = 172.5 M_\odot/\text{pc}^2$ . The total mass is  $M = 1.57 \times 10^{11} M_\odot$  and the tidal radius is  $68.15 r_0$ . We take as time scale the Jeans free-fall time of the core, that is  $t_J = \sqrt{(\pi/(G\rho_0))} \simeq 0.01 H_0^{-1}$ . and  $T = 10 t_J$  as time span for the simulation.

The results in Table I show that coarse-grained observables suffers differently from the large change of  $f$  due to numerical diffusion. While the mass changes only by few percents, the cumulative local change of the energies is ten times as much. The behavior of  $\Delta_K$ , larger at  $t = T/10$  than at  $t = T$ , is due to early fast diffusion in velocity space, which locally heats the system. These results show that it is not wise to trust a numerical VP integration for times too large compared to the natural time scale of the problem at hand.

#### Test 3: Uniform expansion

This third test consists in running a full cosmological simulation, from  $z = 100$  to  $z = 0$ , of the uniform expanding Universe filled with WDM. That is, we set to zero the initial fluctuations  $\delta_i = 0$  and  $u_i = 0$  in eqs. (2.18), (2.19) and (2.20). This is manifestly a stationary solution of the 6-dimensional VP equation in comoving coordinates, Eq. (2.4), since  $\phi$  vanishes and  $f(\mathbf{r}, \mathbf{v}, s = 0)$  in Eq. (2.7) does not depend on  $\mathbf{r}$ . Of course, also the spherically symmetric VP equation (2.12) is satisfied, since the isotropic freeze-out distribution  $f_i$  depends only on  $v^2 = u^2 + \ell^2/r^2$  and

$$\left[ u \partial_r + \frac{\ell^2}{r^3} \partial_u \right] v^2 = 0$$



Hence the test essentially checks how accurately this equation numerically holds in our program. Any error will be converted into small fluctuations, thus generating a fake gravitational force which will in turn amplify the fluctuations, that is the numerical errors. After all, it is at the heart itself of the theory of structure formation that the uniformly expanding solution of the VP equation is unstable. Hence small perturbations are amplified and at the linear level their characteristic amplitude grows proportionally to the scale factor when matter dominates.

For this test  $f^{(e)}$  is just the initial  $f$ ,  $M(r)^{(e)}$  is the background mass  $(4\pi/3)\rho_M r^3$  of Eq. 2.12, while

$$U(r)^{(e)} = -\frac{2\pi}{5}\rho_M a^2 H^2 r^5, \quad K(r)^{(e)} = -U(r)^{(e)} + 2\pi\rho_M \frac{\sigma_0^2}{a^2} r^3.$$

From the numbers in Table I, one sees that the physical instability of the uniform expanding Universe causes a large change in  $f$ , as expected, but the effects of fluctuations on mass and energy profiles do not grow beyond the linear level.

#### IV. MAIN RESULTS

In this section we describe the most important features, according to our simulations, of the gravitational collapse of the WDM halos. We selected many initial fluctuation profiles according to the procedure in Sec. III D and eventually collected 111 collapsed halos at redshift  $z = 0$ . Our results show that basic quantities such as the density and velocities or the virial ratio do stabilize to a large extent as  $z \rightarrow 0$  and show universal properties. This quasi-stationary state is however quite different from naive expectations based on approximate virialization or (local) thermalization arguments.

For simplicity we show only one-dimensional profiles, but the reader should keep in mind that we computed the evolution in superconformal time  $s$  of the full 3-dimensional distribution function  $f(r, u, \ell^2, s)$ . We also recall that the initial velocity dispersion is  $\sigma_0 = 0.025$  km/s, consistent with a thermal relic mass  $m = 1$  keV/ $c^2$  according to Eq. 2.10. Reports on other values for  $\sigma_0$  are provided only in Sec. IV E.

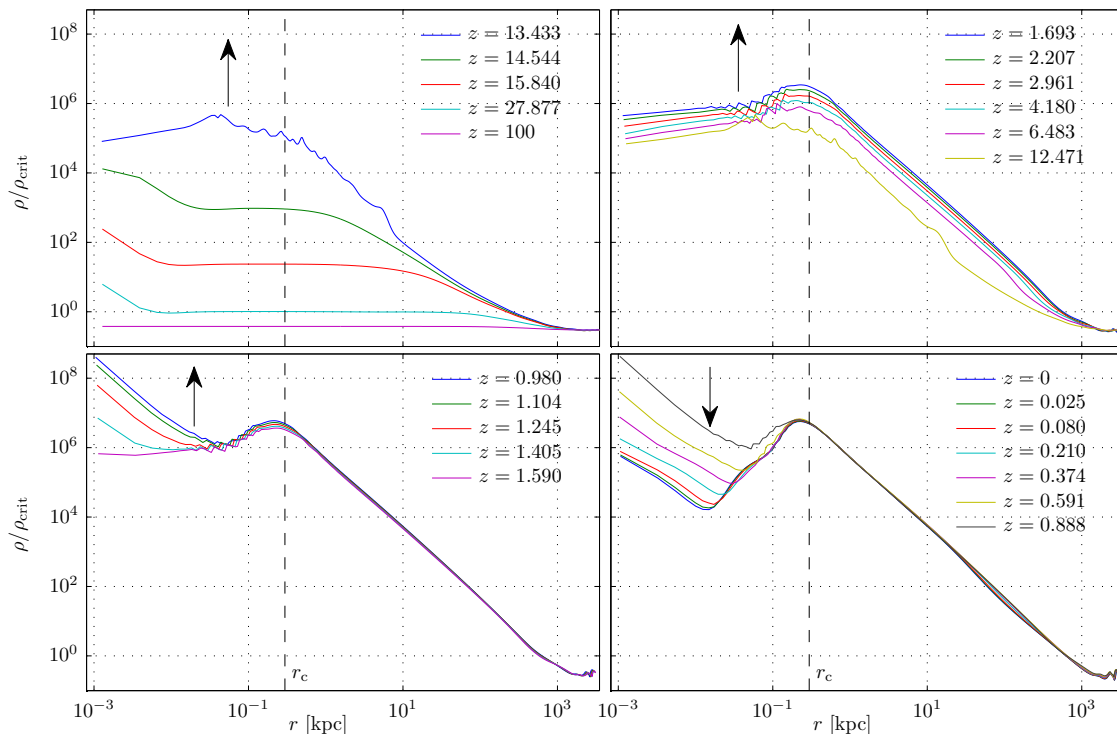


FIG. 2: Evolution of the density profile in the halo example H1. The arrows emphasize the direction of change. The vertical dashed line indicate the position of the core radius  $r_c$  defined in Sec. IV B.

### A. Density and velocities

An example of the evolution of the mass density profile  $\rho(r)$  is depicted in Fig. 2. In this particular case the initial fluctuation profile  $\delta_i(r)$  was selected by prominence within  $R' = 3 \text{ Mpc}$  among the highest ones in the unsmoothed perturbation field. The peak maximum in the origin is  $\delta_i(0) = 0.26$ , while  $M_0 = 4.27 \times 10^{12} M_\odot$ . For ease of reference, let us name this example H1. We could regard H1 as a numerical approximation to the real, nearly spherical and undisturbed collapse as a WDM halo.

Comparing the final density curves of H1 with those in the lower left panel of Fig. 1 one can appreciate the complete similarity, in spite of the large difference in the initial peak heights and shapes. Indeed the cored and peculiarly hollow shape of these plots is the crucial result of our simulations. This shape is universal, in the sense that it is common to all initial overdensity profiles considered. To highlight this fact in the left panel of Fig. 3 we plot the density curve of H1 superimposed to a set, denoted SH1, of 28 similar curves obtained from different initial perturbations. Along the density curve the dots indicate the computation points, that is the cell middlepoints. In the right panel we plot the profiles, that is  $\rho/\rho_{\text{max}}$  vs.  $r/r_{\text{max}}$ , that show a good collapse onto a universal shape.

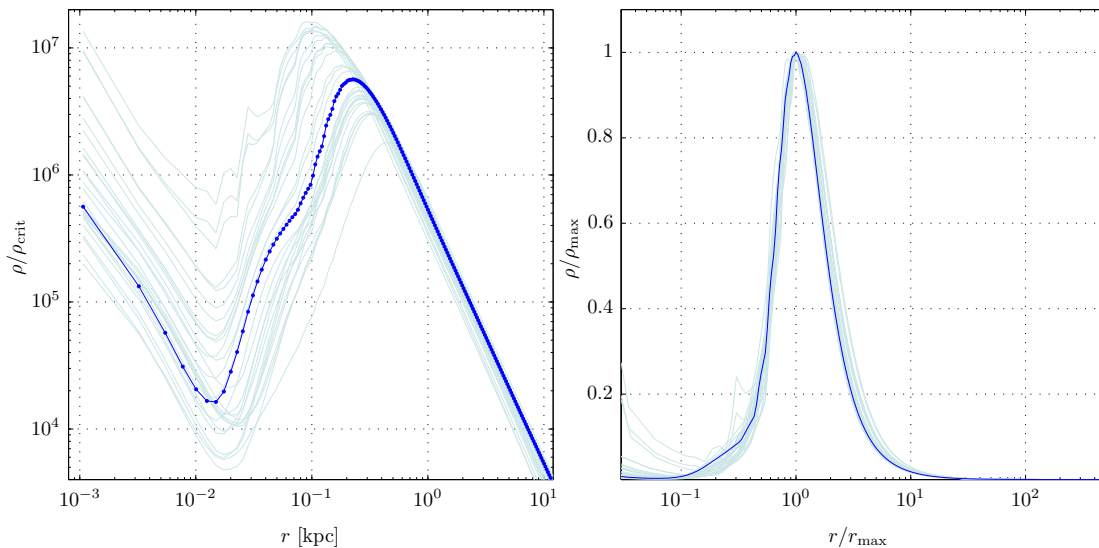


FIG. 3: The  $z = 0$  density of H1 with the explicit indication of the computation points (left panel) and the scaled density (right panel). Paler lines correspond to the set SH1 with other 28 halos obtained from different initial conditions.

Indeed the presence of a maximum value  $\rho_{\text{max}}$  at a non-zero distance  $r_{\text{max}}$  is the most remarkable universal property of  $\rho(r)$ . The values of  $\rho_{\text{max}}$  and  $r_{\text{max}}$  vary instead from halo to halo, depending on the initial overdensity profile that was used to generate them.

Another universal property is the nearly constant logarithmic slope in an extended region on the right of the maximum. This slope stays very close to the value 2, that is  $\rho(r) \sim r^{-2}$ , as can be verified by observing the presence of a clear plateau in the plot of  $r^2 \rho(r)$  vs.  $r$ . The height of the plateau, as well as its extent, are instead halo-dependent features. It is also quite evident that the plateau extension, that is the region where  $\rho(r) \sim r^{-2}$ , is much wider than in the halos of  $N$ -body simulations, a discrepancy most likely due our setup near the boundary of the simulation box.

Clearly  $r_{\text{max}}$  already gives a natural definition of *core radius*, but we will nevertheless provide a slightly different definition in the next section.

It must also be stressed that the history of  $\rho(r)$  is very similar throughout our halo sample, in spite of the differences in the initial  $\delta_i(r)$  profiles, with essentially only two quantitative features that change from one halo to the other. The first is the redshift of rapid formation of the maximum at  $r_{\text{max}}$  (a natural definition of the moment of collapse), signaled by the steep rise in Fig. 4; the second is the value  $\rho_{\text{max}}$  has at a fixed redshift before ( $z = 20$  in Fig. 4). These two features are naturally strongly correlated.

The rather complex motion of the DM fluid can be appreciated in Fig. 5, where the evolution of the average radial velocity  $\bar{u}$  in H1 is depicted. Notice that  $\bar{u}$  vanishes as  $z \rightarrow 0$  in a whole region around the core radius  $r_c \simeq r_{\text{max}}$ , signaling the separation of the core from the outer more diffused halo. Namely, Jeans equation (2.17) nearly holds

around the core boundary and the core in is equilibrium (hydrostatic in fluid viewpoint, dynamic in particle viewpoint) with the rest of the halo.

On the other hand the development, near redshift  $z = 0$ , of a large infall in the outer part of the halo and an outward flux at even larger distances, show that the halo as a whole is not in hydrostatic equilibrium. The outward flux leads to a slight loss of matter.

Also the radial and tangential velocity dispersions of Eq. 2.15 feature a quite complex evolution, shown in Figs. 6 and 7 again for halo H1. One must notice the  $r^{-1}$  decrease of  $\sigma_\theta$  for  $r > r_{\max}$  and its large oscillation at small redshift in the central part of the halo. We find that the pressure, Eq. 2.16), is strongly anisotropic, with the radial component  $P_{rr}$  quite smaller than the tangential component  $P_{\theta\theta}$  in the region where the density grows, a property that can be traced back to the conserved angular momentum. Both components die faster than  $1/r^2$  in the extended region outside the core where  $\rho(r)$  dies as  $1/r^2$  (and therefore the mass grows like  $r$ ), since both velocity dispersions also vanish as  $r$  grows. This is not compatible with Jeans equation (2.17) but is just in keeping with Euler equation (2.14) with  $\partial_t \bar{u} \approx 0$  and  $\bar{u} \partial_r \bar{u} \not\approx 0$ , due to the large infall in the outer part of the halo.

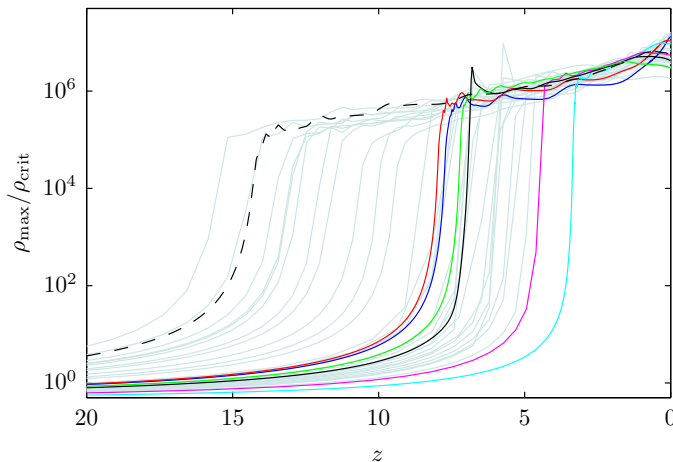


FIG. 4: Evolution for  $20 > z \geq 0$  of the density value on the cell where  $\rho = \rho_{\max}$  at  $z = 0$ . The dashed line corresponds to H1. The lines in full color correspond to the 6 examples of Fig. 1. The paler lines correspond to the 28 halos of SH1; some of them are computed on a coarser grid of redshifts.

If gravitational effects remain the only means to observe DM, then the true DM observable of our numerical halos is the mass  $M(r)$  or, even better, the circular velocity  $v_{\text{circ}}$ , related to the  $M(r)$  by

$$v_{\text{circ}}^2(r) = \frac{GM(r)}{r} = \frac{4\pi G}{3} r^2 \bar{\rho}(r),$$

where  $\bar{\rho}(r)$  is the mean density. Due to the hollow core,  $\bar{\rho}(r)$  is not everywhere larger than  $\rho(r)$ , as it would be if  $\rho(r)$  were monotonically decreasing as in simple equilibrium systems. In particular,  $\bar{\rho}(r)$  is smaller than  $\rho(r)$  where  $\rho(r)$  grows and larger than  $\rho(r)$  beyond a certain point  $r_c > r_{\max}$ , where  $\bar{\rho}(r_c) = \rho(r_c) \equiv \rho_c$  [see the left panel of Fig. 8]. These are universal properties valid for all halos of our simulations.

By construction,  $\rho_c$  is the value at which the density should be cut to replace the hollow core with a constant density core, that is to say,

$$M_c = M(r_c) = \frac{4\pi}{3} \rho_c r_c^3$$

is exactly the mass of the core. But since  $r\bar{\rho}'(r) = 3[\rho(r) - \bar{\rho}(r)]$ , we see that  $r_c$  and  $\rho_c$  are also, perhaps more simply, the position and the value of the maximum of  $\bar{\rho}(r)$ , respectively.

The circular velocity can now be rewritten as

$$v_{\text{circ}}(r) = v_c \frac{r}{r_c} \left[ \frac{\bar{\rho}(r)}{\rho_c} \right]^{1/2}, \quad v_c \equiv v_{\text{circ}}(r_c) = \sqrt{GM_c/r_c}. \quad (4.1)$$

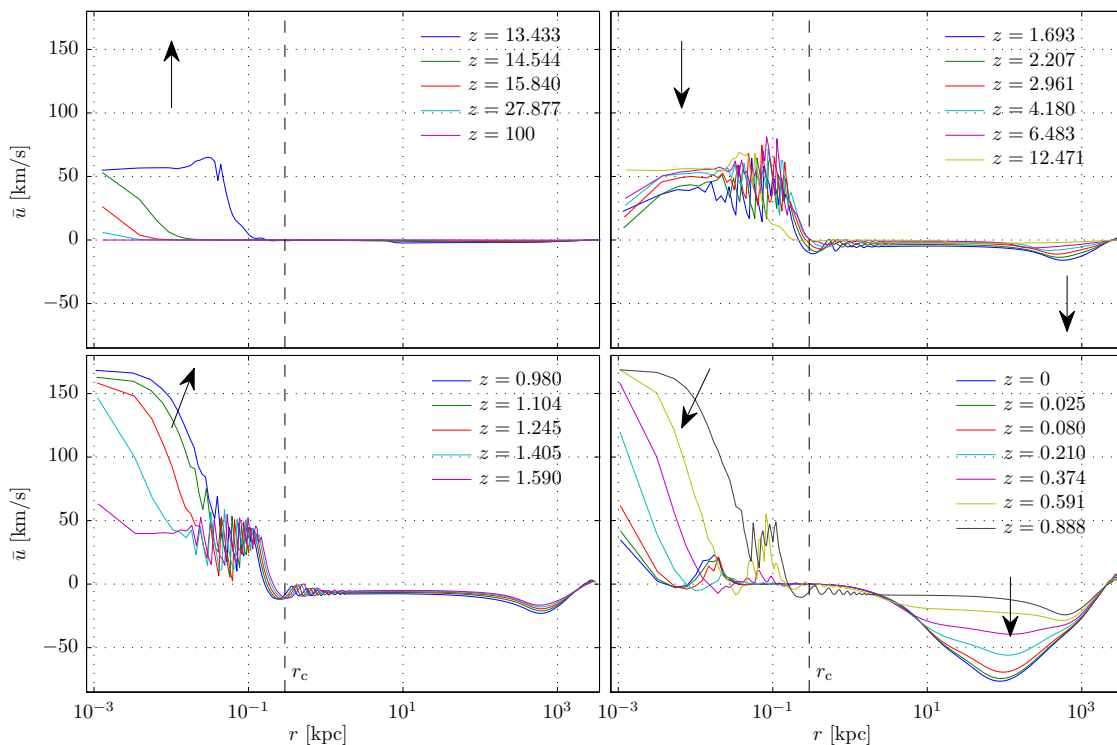


FIG. 5: Evolution of the average radial velocity  $\bar{u} \equiv \langle u \rangle$  in H I. The arrows emphasize the direction of change. Notice the oscillations within the core and the large outer infall.

In the right panel of Fig. 8 we plot the profile  $v_{\text{circ}}(r)/v_c$  vs.  $r/r_c$  for H I (blue curve) as well as the same 28 halos of Fig. 3 (paler curves). The scaling across the core radius is very good and a large region of nearly constant  $v_{\text{circ}}(r)$ , a sort of plateau, can be identified, although not really flat in the logarithmic scale. The plateau heights and shapes remain halo-dependent also after the scaling by  $v_c$ , but the height variation is very limited in a neighborhood of 2. Most importantly, all plateaus are concave, and particularly so where all profiles merge in the scaling region across  $r/r_c = 1$  and coalesce in the universal profile. On the other hand, for  $r/r_c < 1$  this profile drops faster than if the core were bulky rather than hollow, a consequence of the mass deficit in the hollow core.

## B. Core radius, surface density and other parameters

As anticipated by the adopted notation, we take  $r_c$  and  $\rho_c$  as definitions of the *core radius* and *central, or core density*, respectively.

For H I, the halo under closer scrutiny, we find

$$r_c = 0.286 \text{ kpc} \quad , \quad \rho_c = 0.686 M_\odot/\text{pc}^3 \quad (4.2)$$

which are values typical for the core of the DM halo in a dwarf galaxy.

These values should be compared with the results of  $N$ -body simulations of refs. [44, 45], which estimated in few pc the core radius of collapsed halos produced by thermal relics with  $m = 1 \text{ keV}/c^2$ . Those simulations were run with softening lengths of few hundreds pc and different values of initial velocity dispersion  $\sigma_0$ , while keeping the initial conditions typical of  $m = 2 \text{ keV}/c^2$ . [To maintain numbers under control, one has to recall that our  $\sigma_0$  is the 1-dimensional velocity dispersion, larger than the characteristic velocity  $v_0(z=0)$  quoted in ref. [44] by the factor  $B = 2.0768098\dots$  of Eq. (2.9).] At values of  $\sigma_0$  smaller than  $0.025 \text{ km/s}$ , the value consistent with  $m = 1 \text{ keV}/c^2$  and our reference choice, the cores were not resolved, but the density profile was found very close to that of CDM for  $r > 1 \text{ kpc}$ , that is for  $r > 3 r_c$ . The first resolved core was found for  $m = 0.13 \text{ keV}/c^2$  (simulation WDM3 in ref. [44]) with a quoted core radius  $r_{\text{core}} = 0.42 \text{ kpc}$ . Using the data from simulations at higher  $\sigma_0$  and their proximity from below to the theoretical  $Q$ -based upper bound [48],  $r_{\text{core}}$  was extrapolated to be  $\lesssim 10 \text{ pc}$  for  $m \gtrsim 1 \text{ keV}/c^2$ .

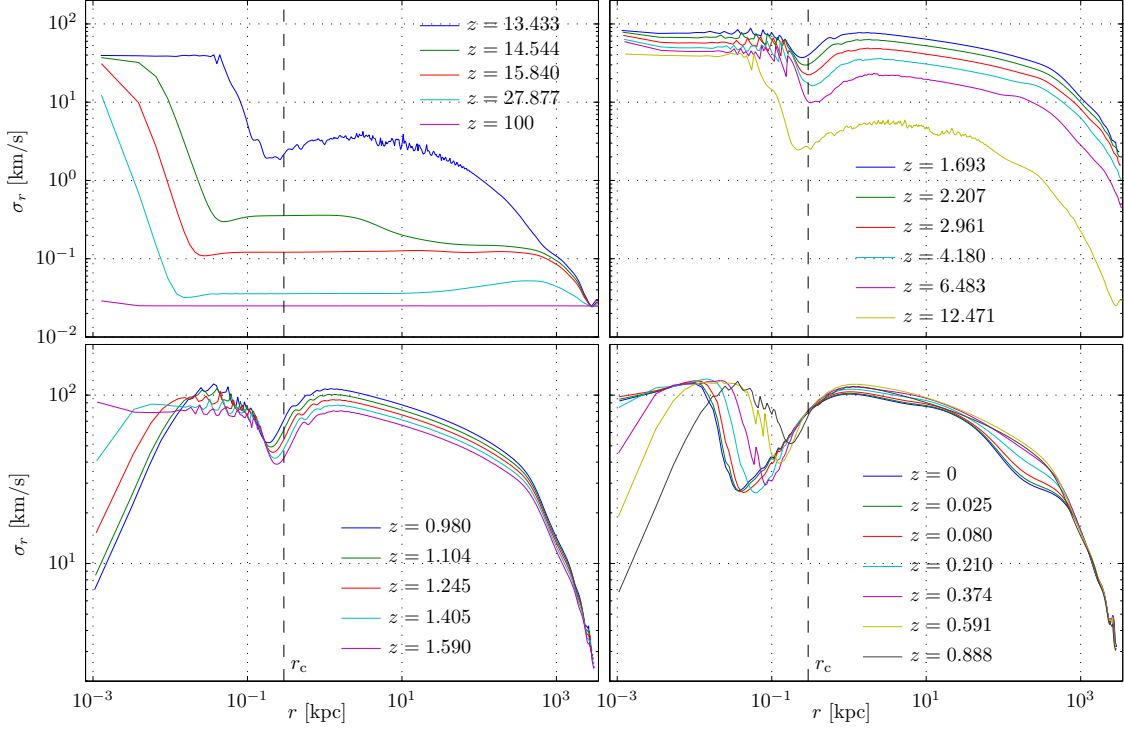


FIG. 6: Evolution of the radial velocity dispersion  $\sigma_r$  in H1. Notice the minimum inside the core and the rise across the region of maximal density.

The discrepancy with our result for H1,  $r_{\text{core}} = r_c = 356$  pc is due the extrapolation procedure (mis-)guided by the  $Q$ -based bound. Indeed, the  $Q$ -based bound is itself based on the apriori assumption mentioned in the Introduction, namely that the isothermal sphere provides a good description of the halo core.

Suppose to try and fit the circular velocity  $v_{\text{circ}}(r)$  of H1 with that of an isothermal sphere, in the hypothesis of knowing  $v_{\text{circ}}(r)$  only outside the core, say  $r > 2r_c$ . The circular velocity  $v_{\text{iso}}(r)$  of the isothermal sphere with King's radius  $r_0$  and central density  $\rho_0$  can be written as

$$v_{\text{iso}}(r) = \sqrt{2} \bar{\sigma} g(r/r_0)$$

where  $\bar{\sigma}$  is the isothermal one-dimensional velocity dispersion

$$\bar{\sigma} = \frac{1}{3} \sqrt{4\pi G \rho_0 r_0^2}.$$

and  $g(x)$  is the well known profile that performs dampened oscillations around unity as  $x \rightarrow \infty$ . In the right panel of Fig. 8 we plot with a dashed line the profile  $1.3 g(x/15)$  vs.  $x = r/r_c$ .

It is natural to start by matching the H1 plateau value of  $v_{\text{circ}}(r)$ , which has roughly the value  $1.8 v_c$ , by setting  $\sqrt{2} \bar{\sigma} \simeq 1.8 v_c$ , or

$$\rho_0 r_0^2 \simeq 4.86 \rho_c r_c^2.$$

It remains to fix the relative distance scale, that is  $r_c/r_0$ . If the plateau were really flat, the best fit would require the limit  $r_0 \rightarrow 0$  yielding the singular isothermal sphere, in order to flatten out the characteristic oscillations of  $v_{\text{iso}}(r)$  for large but finite  $r/r_0$ . Since the plateau is not flat, a better fit could be obtained at some  $r_0 > 0$ , but certainly  $r_0$  must be small enough so that at least the first large oscillation of  $g(r/r_0)$  gets out of the way, as in the right panel of Fig. 8. Since we assumed that  $r = 2r_c$  is the closest we can get to the core and  $x \simeq 30$  is the location of the first minimum of  $g(x)$  on the right of its maximum, we have

$$r_0 \lesssim r_c/15.$$

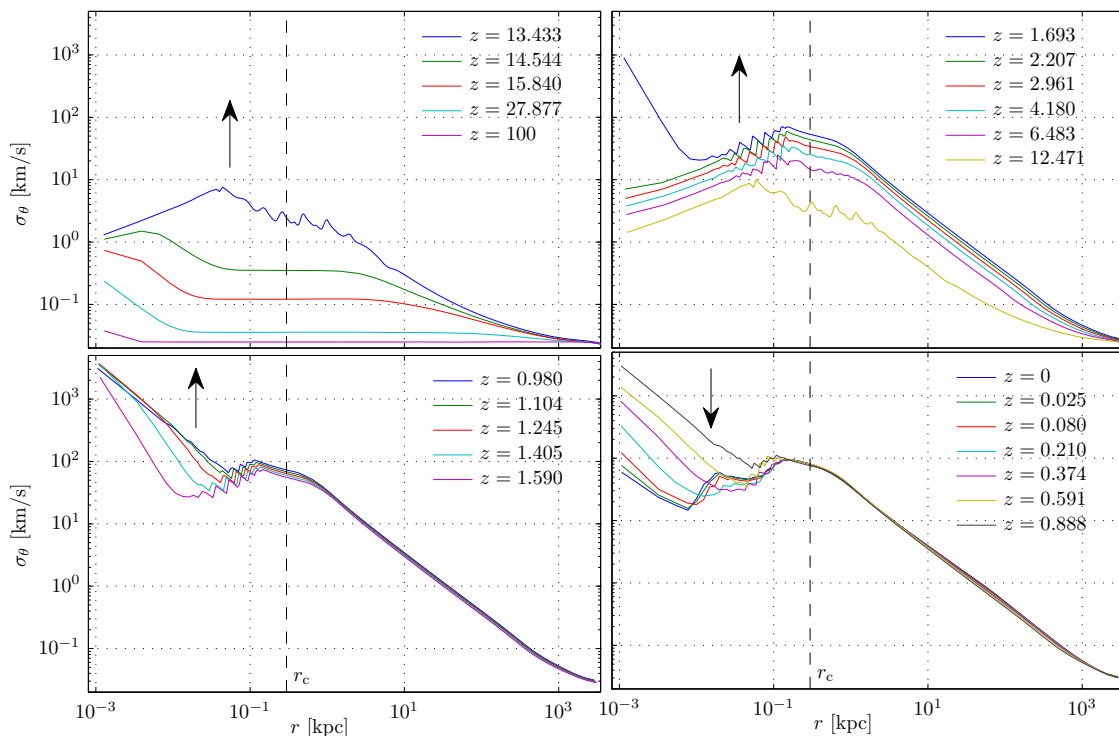


FIG. 7: Evolution of the tangential velocity dispersion  $\sigma_\theta$  in H1. The arrows emphasize the direction of change. Notice the correlation with the density evolution in Fig. 2: when matter contracts it spins faster.

$15 r_0$  is indeed the value at which the density  $\rho_{\text{iso}}(r)$  of the isothermal sphere is declared to enter its mean  $1/r^2$  regime [2]. In the left panel of Fig. 8 we plot  $\rho_{\text{iso}}(r)$  with  $r_0 = r_c/15$  and  $\rho_0 = 4.86 \times 15^2 \rho_c$ .

Given reasonable mock data for the specific halo H1, the fit could probably be improved, but such an exercise is beyond the scope of this discussion, which is to show that the dashed black lines in Fig. 8 provide the natural extrapolations of density and circular velocity profiles when the core is not resolved *and an isothermal sphere is assumed*. Using the values (4.2) of H1 we find

$$\rho_0 \gtrsim 750 M_\odot/\text{pc}^3, \quad r_0 \lesssim 20 \text{ pc},$$

in keeping with the extrapolated results of  $N$ -body simulations in refs. [44, 45], whose quick conclusion was that keV-ranged WDM does not help in solving the core problem of DM halos [87].

We rather conclude that, even when  $N$ -body simulations resolve the core by increasing the initial velocity dispersion, they underestimate the final velocity dispersion in the core region, since not so many “particles” with  $10^5 M_\odot$  mass can fit into a  $10^7 M_\odot$  core. This implies an overestimation of the phase-space density  $Q$  to values close to the theoretical bound, with the proximity holding through the misguided extrapolation. In Sec. IV E we provide data on the relaxation factor  $Z$  of Eq. (4.4) which show that, on the contrary, also in the core region  $Q$  starts dropping very rapidly as the initial velocity dispersion  $\sigma_0$  is decreased below 0.40 km/s, that is when  $m > 0.125 \text{ keV}/c^2$ .

With  $r_c$  and  $\rho_c$  we can compute the so-called *central surface density*  $\mu_c = \rho_c r_c$ . For the case at hand, example H1 with the values as in Eq. 4.2, we find

$$\mu_c = 203 M_\odot/\text{pc}^2 \tag{4.3}$$

in remarkable, but rather puzzling agreement with the observed value  $\mu_{0,\text{obs}} = 140_{-52}^{+83} M_\odot/\text{pc}^2$  [55, 57]. Puzzling because the observed value is obtained by fitting the density of DM halos with the Burkert profile [58]

$$\rho_B(r) = \rho_{0B} B(r/r_{0B}), \quad B(x) = \frac{1}{(1+x)(1+x^2)}$$

which is quite different from the hollow one.

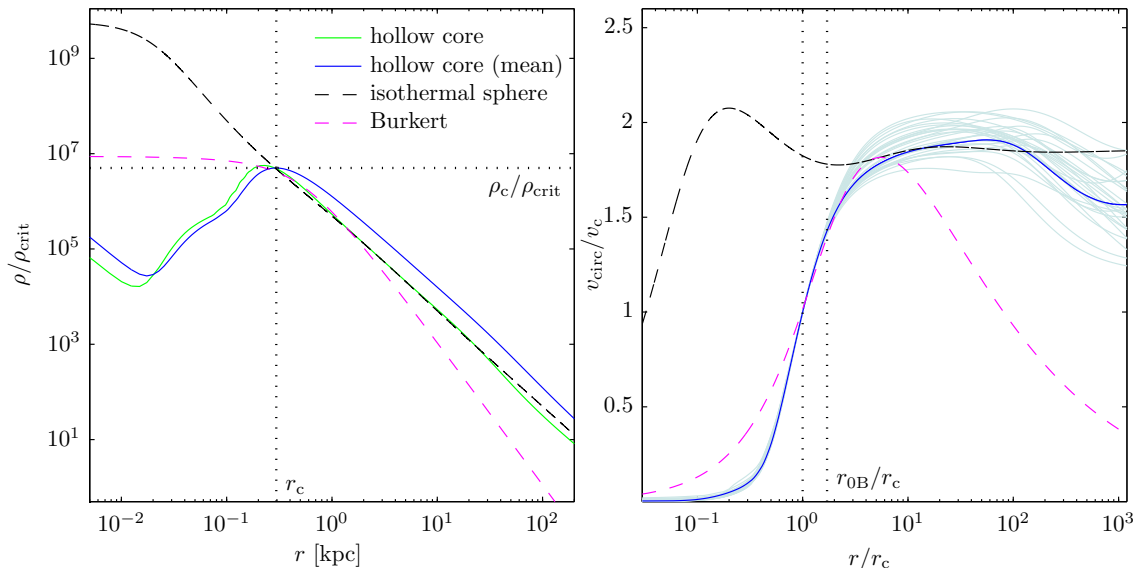


FIG. 8: Left panel: comparison of the hollow density  $\rho(r)$  of H1 with its mean  $\bar{\rho}(r)$ , with the density profile of the isothermal sphere and with the Burkert profile. Right panel: Circular velocity profiles of H1 (blue curve), of the same 28 halos of SH1 (paler curves), of the isothermal sphere and of the Burkert profile. The isothermal sphere is a good fit for  $r > 2r_c$ , the region explored by  $N$ -body simulations. The Burkert velocity profile is a good fit for  $r_c < r < 10r_c$ . Notice that the Burkert core radius  $r_{0B}$  is almost twice  $r_c$  as a direct consequence of the shape of the profiles.

The surface density in refs. [55, 57] is defined as  $\mu_0 = \rho_{0B}r_{0B}$ . It can be estimated for our hollow cores by trying and fit the circular velocity Eq. (4.1) with  $v_{B,\text{circ}}(r)$ , the circular velocity obtained from the Burkert density, that is

$$v_{B,\text{circ}}^2(r) = 2\pi G\mu_0 r_{0B} x^{-1} [\log(1+x) + \frac{1}{2} \log(1+x^2) - \tan^{-1}(x)] , \quad x = r/r_{0B} .$$

The result is depicted by the magenta green lines in Fig. 8. Notice that a good fit is possible only in some finite interval on the right of  $r_c$ , because of the mass deficit of the hollow core and the too long  $r^{-2}$  tail of the diffuse part of the halo. In Fig. 8 the interval, fixed a priori, is  $r_c < r < 10r_c$ . A closer fit in a narrower interval is possible at the price of increasing the gap between  $V_{B,\text{max}}$ , the maximal Burkert circular velocity, and  $V_{\text{max}}$ , the actual maximum of  $v_{\text{circ}}$ . Our choice is just a reasonable compromise. The best fit values are

$$r_{0B} = 1.7r_c = 0.504 \text{ kpc} , \quad \mu_0 = 2.97\mu_c = 603 M_{\odot}/\text{pc}^2 , \quad V_{B,\text{max}} = 58.2 \text{ km/s} ,$$

to be compared with Eq. (4.2), (4.3) and  $V_{\text{max}} = 63 \text{ km/s}$ . The concave shape and good scaling properties of  $v_{\text{circ}}^2(r)$ , quite evident from right panel of Fig. 8, imply that  $\mu_0/\mu_c$  have similar values in all other halos of our sample for any other reasonable choice of fit interval. It is important to notice that  $r_{0B}$  is almost twice  $r_c$ , that is the fit is good also inside the Burkert core, down to almost  $r_{0B}/2$ . This internal fitting further improves as the initial velocity dispersion  $\sigma_0$  increases (see Sec. IV E).

$V_{B,\text{max}}$  can be used to quantify the mass content of our halos, without any reference to the excessively long  $r^{-2}$  tail of the diffuse part. Thus the deviation of  $\mu_0$  from the observed value is a direct measure of their core concentration w.r.t. real DM halos. In the core region, H1 is roughly four times more concentrated than observed DM halos because it has  $\mu_0/\mu_{0,\text{obs}} \simeq 4$ , that is a maximal circular velocity four times larger than the typical real DM halo with the same core size. Moreover, since  $\mu_c$  happens to be very close to  $\mu_{0,\text{obs}}$  (for no obvious reasons, at the moment), we see that also the ratio  $\mu_0/\mu_c$  provides a simple quantitative measure of the basic difference between the hollow-core H1 and real DM halos.

This analysis is the least restrictive, of course, since we are fitting H1 with a Burkert profile only where there the fit can be good, namely for  $0.5r_{0B} \lesssim r \lesssim 5r_{0B}$ . Since the Burkert profile allows very good fits to the circular velocities of real DM halos down to few percents of  $r_{0B}$ , one could say that the hollow-core halos of 1 keV WDM, at least as obtained in our simulations, are ruled out by observations. Still, the closeness of  $\mu_c$  with  $\mu_{0,\text{obs}}$  and the relative smallness of  $\mu_0/\mu_c$  provide a very interesting starting point for further improvements and enhancements.

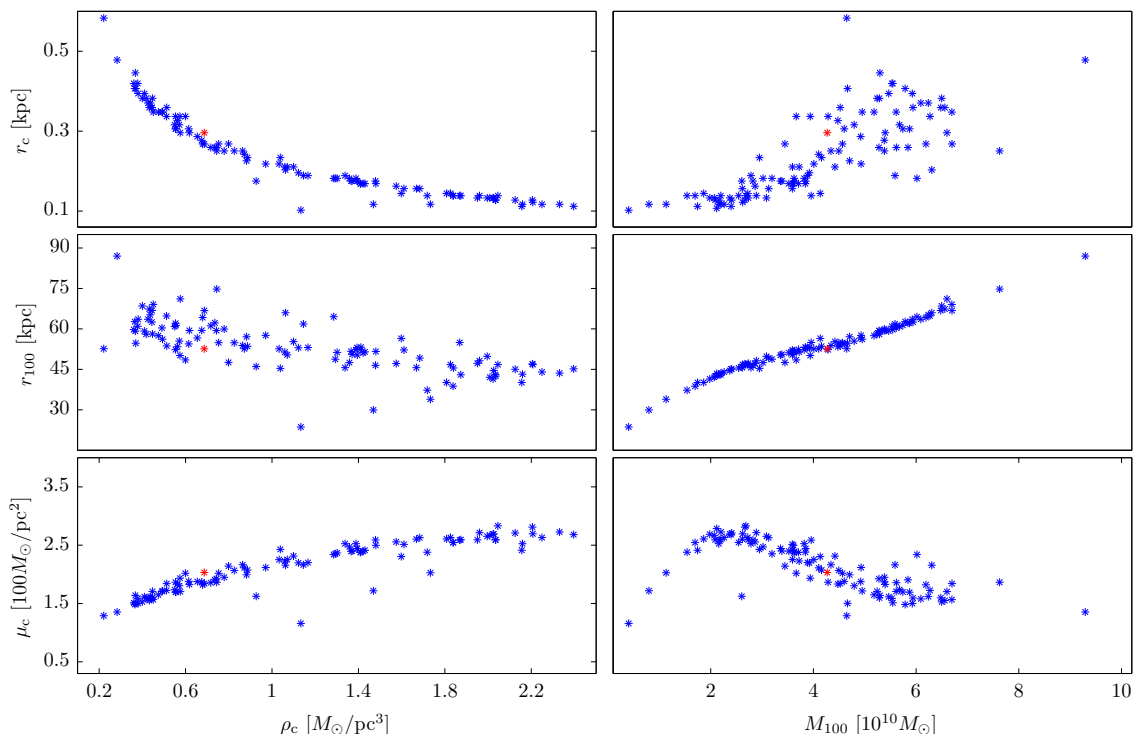


FIG. 9: Scatter plot of the core parameters defined in Sec. IV B as computed in 111 collapse simulations starting from different initial overdensity profiles obtained as in Sec. III D. The red marks correspond to halo H1.

To characterize also the diffuse part of our haloes, we consider the pair  $r_{100}$  and  $M_{\text{halo}} = M_{100}$ . These are the radius at which the density drops to the value  $100 \rho_{\text{crit}}$  and the mass of the halo contained within the corresponding sphere. Since  $r_{100}$  falls always within the region where  $\rho(r) \sim r^{-2}$  and  $M(r) \sim r$ , we expect  $r_{100}$  and  $M_{100}$  to be roughly proportional. We include  $r_{100}$  and  $M_{100}$  for better completeness only, because we have reasons to believe that the excessive length of the  $r^{-2}$  tail is a spurious effect of our initial and boundary conditions.

In Fig. 9 we show some scatter plots of the above parameters over the 111 halos of our sample. In particular, from the scatter plot of  $r_c$  vs.  $\rho_c$  in the upper left panel, one can appreciate more clearly the property already quite evident from the lower left panel of Fig. 1, namely that profiles with a smaller  $\rho_c$  have a larger  $r_c$ .

The lower panels of Fig. 9 exhibits the scatter plot of  $\mu_c$  vs.  $\rho_c$  and vs.  $M_{100}$ . We see that  $\mu_c$  grows quite slowly, by a factor 2, as the central density grows by more than a decade, while it decreases as  $M_{100}$  varies over a decade.

The mean, median, minimal and maximal values of the surface density are, respectively

$$\mu_c \frac{\text{pc}^2}{M_\odot} : 213, 216, 116, 283 \quad , \quad \mu_0 \frac{\text{pc}^2}{M_\odot} : 650, 650, 377, 901 .$$

to be compared with the observed value  $\mu_{0,\text{obs}} = 140^{+83}_{-52} M_\odot / \text{pc}^2$  [55, 57]. The ratio  $\mu_0 / \mu_c$  oscillate between 2.89 and 3.36. The slow decrease of  $\mu_0$  with the halo mass  $M_{100}$  disagrees with the slow increase observed in recent data [86], but our determination of  $M_{100}$  most likely suffers from the biased selection procedure of initial profiles.

### C. Potential and phase-space density

Fig. 10 shows the evolution of the “reduced” gravitational potential  $\phi$  of Eq. (2.5). At redshift  $z = 0$ , wherever the complete background density  $\rho_M - 2\rho_\Lambda$  can be neglected w.r.t. to actual DM density, this potential coincides with the full gravitational potential  $\Phi$ . From Fig. 10 one can see that, in keeping with its coarser-grained nature and unlike the density and especially the velocity profiles, the  $\phi$  profile varies monotonically, smoothly developing a well with a nearly flat bottom in  $\log r$ . This is another clear manifestation of the hollow nature of the core.

The (pseudo) phase-space density is given by  $Q = \rho / \sigma^3$ , where  $3\sigma^2 = \sigma_r^2 + 2\sigma_\theta^2$  is the total velocity dispersion. It provides an estimate of the full distribution function for small velocities. In the purely classical context of this



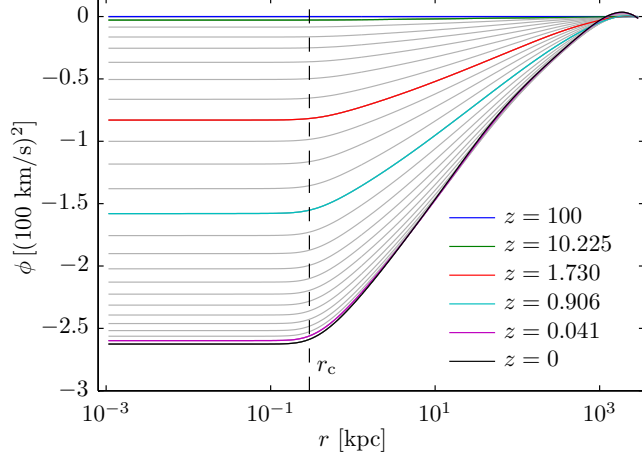


FIG. 10: Evolution of the “reduced” gravitational potential  $\phi$  in the case  $\delta_1(0) = 0.26$ . Gray lines correspond to intermediate redshifts.

work, where values of the distribution function  $f$  are just transported through phase space by the VP equation, any coarse-grained approximation of  $f$  cannot increase during the collapse. Rather, the larger its decrease, the stronger the violent relaxation associated with the collapse (see Sec. IV E). Even if  $Q$  is not exactly a coarse graining of  $f$ , but a ratio of coarse-grained quantities that scales like  $f$ , it is expected to behave similarly.

In Fig. 11 we plot an example of the evolution of (the local version of) the relaxation factor [30]

$$Z(r, z) = \frac{Q(r, z_i)}{Q(r, z)}. \quad (4.4)$$

We see that  $Z(r, 0)$  ranges from values from  $10^3$  to  $10^7$  within the halo, with the smallest value  $Z_{\min}$  attained near the core radius  $r_c$ . Notice also that  $Z(r)$  reaches even larger values near the origin during the second inner infall exhibited in the lower left panel of Figs. 2 and 5.

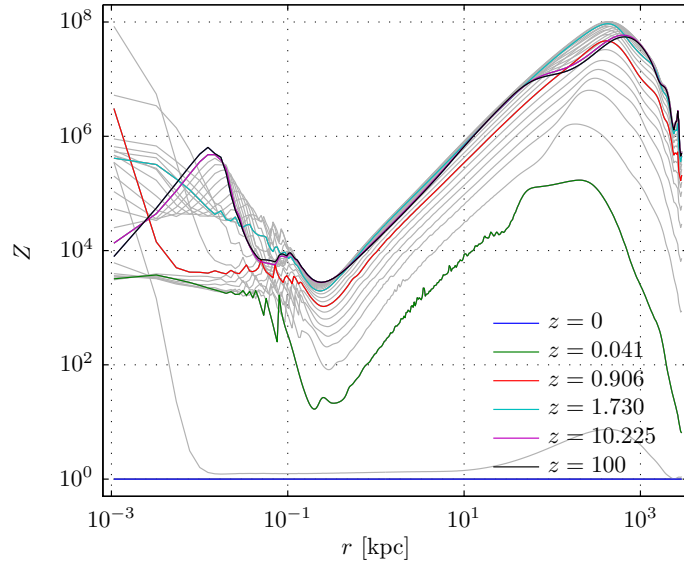


FIG. 11: Evolution of the local relaxation factor  $Z(r)$ , the ratio of the initial value of the (pseudo) phase-space density to its value at redshift  $z$ . Gray lines correspond to intermediate redshifts.

### D. Non-virialized cores

An observer at rest with the collapse center assigns to the DM fluid the kinetic energy density (recall that  $\rho$  is the comoving mass density and that  $3\sigma^2 = \sigma_r^2 + 2\sigma_\theta^2$  is the total comoving velocity dispersion)

$$\begin{aligned}\mathcal{K} &= \frac{1}{2}a^{-3}\rho\langle|\mathbf{v}_{\text{phys}}|^2\rangle = \frac{1}{2}a^{-3}\int d^3v|aH\mathbf{r} + \mathbf{v}/a|^2f(\mathbf{r}, \mathbf{v}, s) \\ &= \frac{1}{2}a^{-5}\rho(a^4H^2r^2 + a^2Hr\langle u\rangle + \langle u\rangle^2 + 3\sigma^2)\end{aligned}$$

Recalling the definitions of  $\Phi_M$  and  $\Phi_\Lambda$ , the gravitational potentials generated by the matter background and the cosmological constant, respectively [see Eq. (2.5)], the same observer assigns to the fluid the potential energy density

$$\mathcal{U} = -a^{-5}\rho r\partial_r(a^2\Phi_M + \phi) + a^{-3}\rho\Phi_\Lambda = -\frac{1}{2}a^{-5}\rho(a^4H^2r^2 + r\phi')$$

where in the last step we used Friedmann equation (2.6). To be precise,  $\mathcal{U}(r)$  is not a real density, since, through the gravitational potential  $\Phi_M$ , it depends on all values  $\rho(r')$  for  $r' \leq r$ . But for our purposes, the important property of  $\mathcal{U}(r)$  is that it does not depend on  $\rho(r')$  for  $r' > r$ , thanks to Gauss' law.

In the uniform Universe, at redshifts large enough that matter fluctuations can be neglected but WDM is already non-relativistic, the two energy densities reduce to

$$\mathcal{U} = -\frac{\rho_M}{2a}H^2r^2, \quad \mathcal{K} = -\mathcal{U} + \frac{3\rho_M}{2a^5}\sigma_0^2$$

and  $\mathcal{K} + \mathcal{U} = 0$  if  $\sigma_0 = 0$ , as in CDM, consistently with the assumed open and flat Universe. Anyway, a nonzero  $\sigma_0$  does not spoil flatness, since it contributes a negligible fraction of the total kinetic energy at large distances. However, the kinetic energy density due to the velocity dispersion dominates at short distances, since the Hubble flow and the gravitational self-interaction become negligible as  $r \rightarrow 0$ . In other words, in the central region of the future collapse the kinetic energy initially overwhelms the potential energy as the  $r$ -dependent initial virial ratio

$$W(r) = \frac{2K(r)}{-U(r)} = \frac{2\int_0^r dr' r'^2 \mathcal{K}(r')}{-\int_0^r dr' r'^2 \mathcal{U}(r')} = 2 + \frac{10\sigma_0^2}{a^4H^2r^2}$$

diverges as  $r \rightarrow 0$ . This fact is only slightly perturbed by the initial matter fluctuations, such as those at  $z = z_i = 100$ , the initial redshift of our setup. In the subsequent gravitational collapse triggered by those fluctuations,  $W(r)$  changes instead dramatically.

The common lore on the evolution of  $W(r)$ , mostly based on the radial collapse model of CDM, envisage a violent relaxation by which the halo is formed as a gravitationally bound system, while most matter that is too energetic is lost. The halo is thus left in a quasi-stationary state that is to a large degree virialized, in the sense that  $W(r) \sim 1$  for  $r_c < r < r_{\text{vir}}$ , where  $r_c$  is the core radius and  $r_{\text{vir}}$  is the virial radius, beyond which matter is typically not in a quasi-stationary state and which could be used to define the halo border. Thus the system should be more equilibrated if not even thermalized, the closer to the origin one gets. At small distances, the phase-space distribution function should then tend to an ergodic form which depends only of the one-particle energy corresponding to the quasi-stationary self-consistent potential. The halo density  $\rho(r)$  is then expected to monotonically decrease away from the origin. In this respect, angular momentum has received attention mostly as a source of corrections to the radial infall model (see *e.g.* [88] and references therein).

Our numerical results clearly put forward quite a different scenario for spherically symmetric WDM collapses. The collisionless, non-dissipative VP dynamics, the conservation of angular momentum and the large values of the initial  $W(r)$  (see discussion in the Sec. IA) are in our opinion the theoretical basis of our findings, although we do not attempt here any quantitative theoretical analysis. The evolution of the virial ratio  $W(r)$ , shown in Fig. 12, features an excess of kinetic energy at small distances which gets somehow trapped well inside the halo as the density peak rises at  $r = r_c$ .  $W(r)$  is stabilizing, as expected in a quasi-stationary state, although with more fluctuations than density or potential. Yet a full plateau of very high  $W(r)$  values remains at  $z = 0$  inside the core, clearly exceeding the power law  $(r/r_c)^2$  proper of equilibrium systems. To remark this fact, we have plotted also the virial ratio of an isothermal sphere with the same core size of H1. Outside the core  $W(r)$  quite slowly decreases reaching values of order one far away from the core. Thus the halo core is hollow and really not virialized.

It is conceivable that this quasi-stationary state is only metastable and that the excess kinetic energy might eventually escape, together with a certain amount of matter and angular momentum. This certainly does not happen

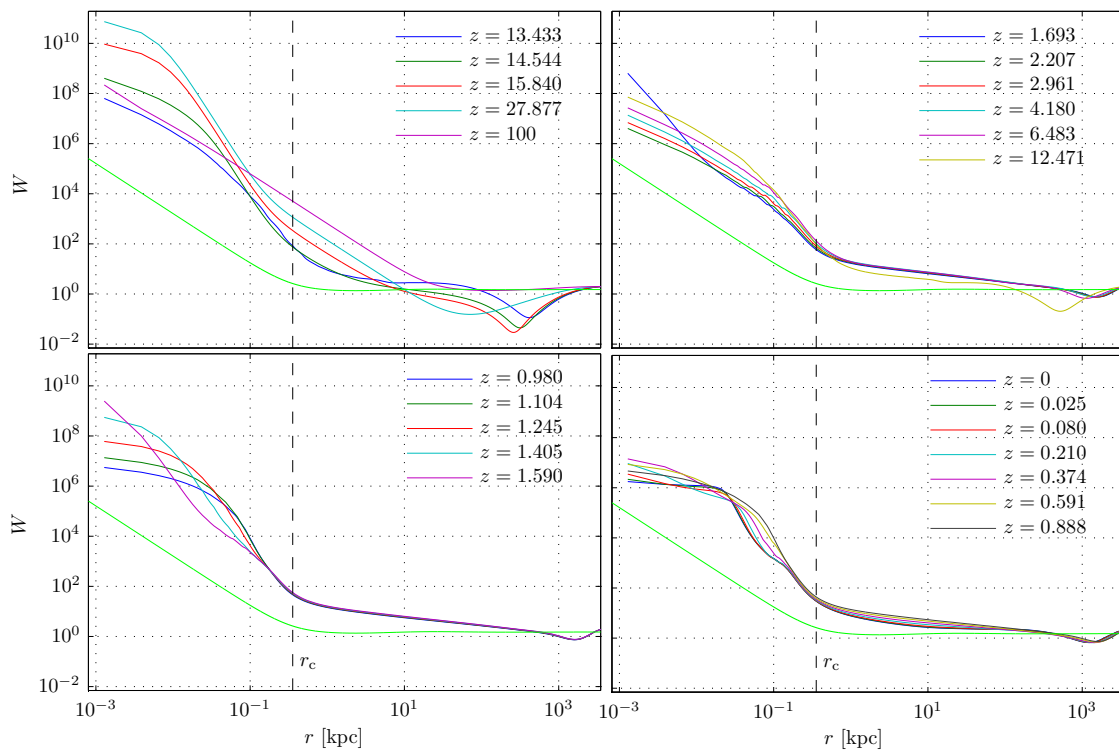


FIG. 12: Evolution of local virial ratio  $W(r)$  in H I, the same halo of Fig. 2 and Figs. 5–7. The bright green line represents the virial ratio of an isothermal sphere with the same core size.

within the finite amount of time available from the initial redshift  $z = 100$  to  $z = 0$ . It would be interesting to find the time scale of the above energy loss, but this is beyond the scope of this work and perhaps beyond our numerical possibilities, because of the unavoidable diffusion and dissipation of VP solvers. Moreover, the large tangential motions inside the core of the collapsing halo and the relatively large value of  $Q_{\text{prim}}$ , as discussed in the Introduction, suggest that a proper quantum treatment of angular momentum could be necessary to achieve better quantitative agreement with observations.

As mentioned above, the virial ratio  $W(r)$  decreases quite slowly as  $r$  grows. If we define the virial ratio  $r_{\text{vir}}$  as the distance at which  $W(r)$  crosses unity, we find on average values forty times larger than  $r_{100}$ . This rather unphysical situation is due to the excessive extension to large distances of the  $1/r^2$  decrease of the density. The latter is probably due to a bias in our method of selecting the initial overdensity profiles, leading to an insufficient matter outflow. Improvements in this respect are certainly necessary, but the hollow core structure can hardly depend on the lack of a significantly faster density decrease in the halo outskirts. Most likely, a faster decrease might enhance the core size, rather than reduce it.

### E. Hollow cores and initial velocity dispersion

It is very interesting to investigate what happens when  $\sigma_0$  is varied. In Fig. 13 we plot the  $z = 0$  densities for five increasing values of  $\sigma_0$ , from  $\sigma_0 = 0.025$  km/s to  $\sigma_0 = 0.4$  km/s, obtained always from the same initial fluctuation  $\delta_i(r)$  of halo H I. To decrease  $\sigma_0$  in our numerical treatment of the VP equation is definitely more difficult, since smaller  $\sigma_0$  implies larger, and very fast increasing, dynamical range in the collapse. In other words, more violent relaxation. This can be appreciated from the second column of Table II, which reports the minimal value  $Z_{\text{min}}$  of the local relaxation factor  $Z(r, 0)$  of Eq. (4.4).

Let us first notice that using the  $m - \sigma_0$  relation, Eq. 2.10, the value  $\sigma_0 = 0.4$  km/s corresponds to  $m = 0.125$  keV/ $c^2$ . In turns, this mass corresponds to the  $N$ -body simulation WDM3 of ref. [44]. One can check that their WDM3 density profile agrees quite well with our hollow  $\rho(r)$  for  $r \gtrsim 1$  pc, on the right of the maximum. This shows that, on the common domain of validity,  $N$ -body simulations and direct VP integration agree, as far as the mass density is concerned.

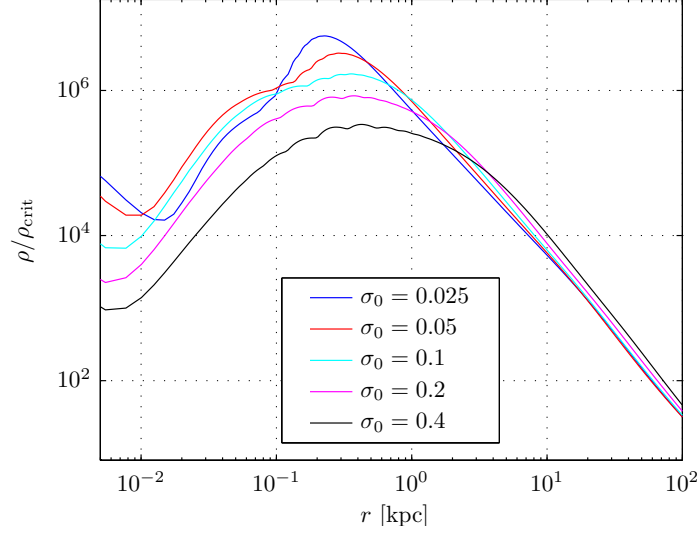


FIG. 13: Density curves at redshift  $z = 0$  for different values of the initial velocity dispersion  $\sigma_0$ , in km/s, but for the same fluctuation profile  $\delta_i(r)$  of halo H1.

$\sigma_0$ s/km	$Z_{\min}$	$r_c/\text{pc}$	$\mu_c \text{ pc}^2/M_\odot$	$V_{\max}$ s/km	$r_{0\text{B}}/\text{pc}$	$\mu_0 \text{ pc}^2/M_\odot$	$V_{\text{B,max}}$ s/km	$mc^2/\text{keV}$
0.025	2813	296	203	63	504	603	58.2	1
0.05	533	413	166	67.9	725	517	65.9	0.594
0.1	96.8	502	117	73.3	1100	415	72.4	0.353
0.2	17.9	566	68.5	78.7	1768	294	77.5	0.210
0.4	4.37	598	33.6	83.6	2939	188	79.8	0.125

TABLE II: Parameter values for halo H1 at different values of the initial velocity dispersion  $\sigma_0$ . In the last column the equivalent WDM mass according to Eq. (2.10).

Fig. 13 and Table II show that the overall size of the core increases with  $\sigma_0$ , as is natural to expect. Maybe less obvious is the peak broadening, that progressively makes the notion of hollowness less appropriate and harder to detect with low-resolution means. In other words, the second length scale of the hollow core, the hollowness scale, grows to values comparable to the first scale  $r_c$ . Notice that  $r_c$ , as defined in Sec IV B, does not grow very much, while  $r_{0\text{B}}$ , the core radius of the Burkert fit, grows almost linearly with  $m$ . Moreover, both  $\mu_c = \rho_c r_c$  and  $\mu_c = \rho_{0\text{B}} r_{0\text{B}}$  considerably decreases, roughly maintaining their ratio constant.

From the data in Table II we can write to a good approximation

$$\mu_c \frac{\text{pc}^2}{M_\odot} \simeq 205 - 43.6 y, \quad \mu_0 \frac{\text{pc}^2}{M_\odot} \simeq 614 - 105 y, \quad y = \log_2 \left( \frac{40 \sigma_0}{\text{km/s}} \right) = -\frac{4}{3} \log_2 \left( \frac{mc^2}{\text{keV}} \right)$$

and

$$\frac{r_{0\text{B}}}{\text{pc}} = 134 + 348 \frac{\text{keV}}{mc^2}. \quad (4.5)$$

Thus, baldly extrapolating to larger values of the WDM mass, we obtain

$$\begin{aligned} \mu_c &= 263 M_\odot/\text{pc}^2, & \mu_0 &= 754 M_\odot/\text{pc}^2, & r_{0\text{B}} &= 355 \text{ pc} & \text{when } m &= 2 \text{ keV}/c^2. \\ \mu_c &= 308 M_\odot/\text{pc}^2, & \mu_0 &= 855 M_\odot/\text{pc}^2, & r_{0\text{B}} &= 239 \text{ pc} & \text{when } m &= 3.3 \text{ keV}/c^2. \end{aligned}$$

Since  $\mu_{0,\text{obs}} = 140_{-52}^{+83} M_\odot/\text{pc}^2$ , we see that the core of H1 would have a surface density (or surface gravity acceleration, since the two are proportional) roughly 6 times larger than real DM halos when  $m = 3.3 \text{ keV}/c^2$ . Taking into account that this applies to pure WDM collapse (that is with no baryon feedback of any type) and within a purely classical

approach (probably a more relevant limitation), we consider this a very good starting point for the improvements outlined in the Introduction.

The last row in Table II shows values of  $r_{0B}$ ,  $\mu_0$  and  $V_{B,max}$  in very good agreement with observations. The corresponding mass,  $m = 0.125 \text{ keV}/c^2$ , is however too small w.r.t. the constraints from large-scale structure.

As a matter of fact, it is also too small w.r.t. the value  $m = 1 \text{ keV}/c^2$  used in the matter power spectrum to generate the fluctuation field from which the initial profile was drawn. We cannot pretend to realistically lower the surface density of one given halo by just raising  $\sigma_0$ , while keeping fixed the initial overdensity profile. Larger  $\sigma_0$  implies more free-streaming in the linear regime of gravitational clustering, with the associated small-scale depression of the matter power spectrum. Thus, a fluctuation profile that was generic at  $\sigma_0 = 0.025 \text{ km/s}$ , could be practically impossible at  $\sigma_0 = 0.4 \text{ km/s}$ . This so-called *catch 22* of WDM, already mentioned in the Introduction, was pointed out already in ref. [44], on the basis of the results of  $N$ -body simulations. However, in ref. [44], the scaling of the core size with the mass was determined to be  $r_{core} \sim m^{-2}$ , while we find the relation (4.5) for the Burkert core radius and an even slower decrease for  $r_c$ . Once extrapolated to  $m = 1 \text{ keV}/c^2$ , the scaling  $r_{core} \sim m^{-2}$  leads to core sizes around 10 pc instead of several hundreds, as we find.

The incorrect scaling  $r_{core} \sim m^{-2}$  can be traced to the underestimation of the relaxation factor  $Z(r, 0)$ , that is the overestimation of the pseudo phase-space density  $Q(r)$ . The smallest value  $Z_{min} = 4.37$  in the second column of table Table II, which corresponds to a value of the mass quite close to simulation WDM3 of ref. [44], implies that  $Z_{min}$  will be even closer to unity, its theoretical minimum, for smaller masses. Indeed the WDM  $N$ -body simulations of ref. [44, 45] could resolve the core only for such masses and found  $Q$  in the core very close to its theoretical maximum. But the explosive growth of  $Z_{min}$  in the second column of table Table II shows that their extrapolation of  $Q$  to larger masses was ill founded.

### Acknowledgments

The author is deeply indebted to H.J. de Vega and N.G. Sanchez for many illuminating discussions and for the kind hospitality in the Observatoire de Paris and the Chalonge School events, where basic motivations were laid down and the development of fruitful ideas was initiated.

The author thankfully acknowledges the computer resources and technical support provided by the Physics Department and the INFN section of the University of Milano-Bicocca.

- 
- [1] D. Lynden-Bell, R. M. Lynden-Bell, MNRAS 181, 405 (1977).
  - [2] J. Binney, S. Tremaine, "Galactic Dynamics", Princeton Univ. Press, Princeton, USA (2008).
  - [3] T. Padmanabhan, Phys. Rep. 188, 285 (1990).
  - [4] S. J. Aarseth, "Gravitational N-Body Simulations: Tools and Algorithms", Cambridge Univ. Press, Cambridge, UK, (2003).
  - [5] S.D.M. White, M.J. Rees, MNRAS 183 341 (1978).
  - [6] C.S. Frenk, S.D.M. White, Ann. der Physik 524, 507 (2012).
  - [7] G. Kauffman, S.D.M. White, B. Guiderdoni, MNRAS 264, 201 (1993).
  - [8] B. Moore *et al.*, ApJ. Lett. 524, L19 (1999).
  - [9] A. Klypin *et al.* ApJ 522, 82 (1999); ApJ 523, 32 (1999).
  - [10] S. Ghigna *et al.* ApJ 544, 616 (2000).
  - [11] B. Willman *et al.* MNRAS 353, 639 (2004).
  - [12] J.F. Navarro, C.S. Frenk, S. White, MNRAS 462, 563 (1996).
  - [13] Y. Hoffman *et al.* ApJ 671, 1108 (2007).
  - [14] B. Moore, *et al.* MNRAS 310, 1147 (1999);
  - [15] R. F. G. Wyse, G. Gilmore, IAU Symposium, Vol. 244, p. 44-52 (2007), arXiv:0708.1492.
  - [16] P. Salucci *et al.* MNRAS 378, 41 (2007);
  - [17] G. Gilmore *et al.*, ApJ 663, 948 (2007).
  - [18] P. Salucci, Ch. Frigerio Martins, EAS Publications Series, 36, 2009, 133-140.
  - [19] J. van Eymeren *et al.* A & A 505, 1-20 (2009).
  - [20] M. Walker, J. Peñarrubia, ApJ 742, 20 (2011).
  - [21] S. Mashchenko, J. Wadsley, H.M.P. Couchman, Science 319, 174 (2008).
  - [22] F. Governato *et al.*, Nature 463, 203 (2010).
  - [23] F. Governato *et al.*, MNRAS 422, 1231 (2012).
  - [24] S. Garrison-Kimmel *et al.* MNRAS 433, 3539 (2013).
  - [25] F. Marinacci *et al.* MNRAS 437, 1750 (2014).

- [26] S. Colombi, S. Dodelson, and L. M. Widrow, *ApJ* 458, 1 (1996).
- [27] P. Bode, J.P. Ostriker, N. Turok, *ApJ* 556, 93 (2001).
- [28] V. Avila-Reese *et al.*, *ApJ* 559, 516 (2001).
- [29] D. Boyanovsky, H.J. de Vega, N.G. Sanchez, arXiv:0710.5180, *Phys. Rev. D* 77, 043518 (2008).
- [30] H.J. de Vega, N.G. Sanchez, arXiv:0901.0922, *MNRAS*. 404, 885 (2010).
- [31] R.E. Smith, K. Markovic, *Phys. Rev. D* 84, 3507 (2011).
- [32] N. Menci, F. Fiore, A. Lamastra, *MNRAS* 421, 2384 (2012).
- [33] P. Colín, O. Valenzuela, V. Avila-Reese, *Ap J*, 542, 622 (2000).
- [34] J. Sommer-Larsen, A. Dolgov, *ApJ* 551, 608 (2001).
- [35] L. Gao and T. Theuns, *Science*, 317, 1527 (2007).
- [36] A. V. Tikhonov *et al.*, *MNRAS*, 399, 1611 (2009).
- [37] J. Zavala *et al.*, *ApJ* 700, 1779 (2009).
- [38] E. Papastergis *et al.*, *ApJ* 739, 38 (2011).
- [39] M. R. Lovell *et al.*, *MNRAS*, 420, 2318 (2012).
- [40] V. Avila-Reese *et al.*, *ApJ* 559, 516 (2001).
- [41] P. Colín, O. Valenzuela, V. Avila-Reese, *ApJ*, 673, 203 (2008).
- [42] F. Villaescusa-Navarro and N. Dalal, *JCAP* 03, 024 (2011).
- [43] J. Viñas, E. Salvador-Solé, A. Manrique, arXiv:1202.2860.
- [44] A. Macciò *et al.*, *MNRAS* 424, 1105 (2012); *MNRAS* 428, 3715 (2013).
- [45] S. Shao *et al.*, *MNRAS* 430, 2346 (2013).
- [46] M.R. Lovell *et al.*, *MNRAS* 439, 300 (2014).
- [47] S. Tremaine, J.E. Gunn, *Phys. Rev. Lett.* 42, 407 (1979).
- [48] C.J. Hogan, J.J. Dalcanton, *Phys. Rev. D* 62, 063511 (2000),
- [49] S. Tremaine, M. Henon, D. Lynden-Bell, *MNRAS* 219, 285 (1986).
- [50] J. Madsen, *Phys. Rev. Lett.* 64, 2744 (1990);
- [51] J. J. Dalcanton, C. J. Hogan, *ApJ* 561, 35 (2001).
- [52] J. Madsen, *Phys. Rev. D* 64, 027301 (2001).
- [53] A. Boyarsky, O. Ruchayskiy, D. Iakubovskiy, *JCAP* 3, 5 (2009),
- [54] J. Kormendy, K.C. Freeman, *IAU Symposium, Sydney*, 220, 377 (2004),
- [55] M. Spano *et al.*, *MNRAS* 383, 297 (2008)
- [56] F. Donato *et al.*, *MNRAS* 397, 1169 (2009).
- [57] P. Salucci *et al.*, *MNRAS* 420, 2034 (2012).
- [58] A. Burkert, *ApJ* 447, L25 (1995).
- [59] H.J. de Vega, N.G. Sanchez, arXiv:1304.0759.
- [60] K.N. Abazajian, *Phys. Rev. Lett.* 112, 161303 (2014).
- [61] M. Viel, G.D. Becker, J.S. Bolton, M.G. Haehnelt, *Phys. Rev. D* 88, 043502 (2013).
- [62] K. Yoshikawa, N. Yoshida, M. Umemura, *ApJ* 762, 116 (2013).
- [63] D. Boyanovsky, *Phys. Rev. D* 78, 103505 (2008).
- [64] K. Petraki, *Phys. Rev. D* 77, 105004 (2008);
- [65] D. Boyanovsky, J. Wu, *Phys. Rev. D* 83, 043524 (2011).
- [66] H.J. de Vega, N.G. Sanchez, *Phys. Rev. D* 85, 043516 (2012); 85, 043517 (2012).
- [67] D. Boyanovsky, *Phys. Rev. D* 83, 103505 (2011).
- [68] C. Destri, H.J. de Vega, N.G. Sanchez, *New Astr.* 22, 39 (2013); *Astrop. Phys.* 46, 14 (2013).
- [69] P.L. Biermann, H.J. de Vega, N.G. Sanchez, arXiv:1305.7452.
- [70] S. Dodelson, L. M. Widrow, *Phys. Rev. Lett.* 72, 17 (1994).
- [71] M. Shaposhnikov, I. Tkachev, *Phys. Lett. B* 639, 414 (2006).
- [72] X. Shi, G.M. Fuller, *Phys. Rev. Lett.* 82, 2832 (1999).
- [73] W. Braun and K. Hepp, *Commun. Math. Phys.* 56, 101 (1977).
- [74] D. Lynden-Bell, *MNRAS* 136, 101 (1967).
- [75] P.H. Chavanis, J. Sommeria, *MNRAS* 296, 569 (1998).
- [76] A. Antoniazzi *et al.*, *Phys. Rev. E* 75, 011112 (2007).
- [77] Y. Levin, R. Pakter, F.B. Rizzato, *Phys. Rev. E* 78, 021130 (2008).
- [78] F. Sylos Labini, *MNRAS* 423, 1610 (2012).
- [79] F. Bernardeau, arXiv:1311:2724.
- [80] A. Lapi, A. Cavaliere, *ApJ* 743, 127 (2011).
- [81] F. Filbet, E. Sonnendrücker, *Comp. Phys. Comm.* 150, 247 (2003).
- [82] R. LeVeque, "Finite Volume Methods for Hyperbolic Problems" Cambridge Univ. Press, Cambridge, UK, (2002).
- [83] J. M. Bardeen, J. R. Bond, N. Kaiser, A. S. Szalay, *ApJ* 304, 15 (1986).
- [84] A. Lewis, A. Challinor, <http://camb.info>.
- [85] C. Destri, H.J. de Vega, N.G. Sanchez, *Phys. Rev. D* 88, 083512 (2013).
- [86] A. Boyarsky *et al.*, *Phys. Rev. Lett.* 104, 191301 (2010).
- [87] A. Schneider *et al.*, *MNRAS Lett.* 441 L6, 2014.
- [88] P. Zukin, E. Bertschinger, *Phys. Rev D* 82, 104044 (2010).